Energy Storage Materials 90 (2026) 105375

Contents lists available at ScienceDirect

Energy Storage Materials

journal homepage: www.elsevier.com/locate/ensm

Threshold-triggered redox modulation maximizing initial Na^+ extraction in Fe–Mn-dominant P2-type Na-layered cathodes

Sunghyun Lim [a,b], Jeongwoo Kim [a,b], Bonyoung Ku [a,b], Myungeun Choi [a,b], Hoseok Lee [b,c], Junha Kwon [a,b], Lahyeon Jang [a,b], Taegyu Kim [b,c], Hun-Gi Jung [d,e], Junyoung Mun [b,c,d,e], Jongsoon Kim [a,b,c,d,*]

[a] Department of Energy Science, Sungkyunkwan University, Suwon, 16419, Republic of Korea
[b] SKKU Institute of Energy Science and Technology (SIEST), Sungkyunkwan University, Suwon, 16419, Republic of Korea
[c] Department of Future Energy Engineering, Sungkyunkwan University, Suwon, 16419, Republic of Korea
[d] KIST-SKKU Carbon-Neutral Research Center, Sungkyunkwan University, Suwon 16419, Republic of Korea
[e] Energy Storage Research Center, Korea Institute of Science and Technology, Seoul 02792, Republic of Korea

ARTICLE INFO

Keywords:
P2-layered oxides
Oxygen redox
Redox modulation
Sodium-ion batteries

ABSTRACT

Layered P2-type oxides are promising cathodes for sodium-ion batteries (SIBs); however, in Co-free, Ni-minimized Fe–Mn-based systems, their practical energy density is intrinsically limited by insufficient Na^+ extraction during the initial charge. Because these compositions rely predominantly on transition-metal (TM)-based cationic redox, the cyclable Na inventory is fundamentally constrained by the intrinsic TM redox capacity, resulting in limited charge capacity and suppressed energy density. Here, we demonstrate threshold-governed structure-coupled redox modulation, which overcomes this intrinsic limitation in Co-free, Ni-minimized P2-type Fe–Mn-based layered cathodes. Once the substitution level exceeds a critical threshold, the redox mechanism transitions from predominantly TM-dominated processes to cooperatively stabilized oxygen-involved redox. This transition expands the thermodynamically accessible Na^+ extraction window while maintaining structural integrity. As a result, the modulated cathode, P2-$Na_{0.6}[Ni_{0.1}Fe_{0.1}Mn_{0.65}Mg_{0.15}]O_2$, delivers an increased charge capacity while bringing the initial Coulombic efficiency (ICE) close to unity (from ~124.60% to ~99.95%), along with a higher average discharge voltage (~3.304 V) compared with pristine P2-type $Na_{0.6}[Ni_{0.1}Fe_{0.1}Mn_{0.8}]O_2$, leading to substantially enhanced reversible capacity and practical energy density in full-cell systems. *Operando* structural characterization combined with first-principles calculations reveals that this performance enhancement originates from suppressed high-voltage phase evolution and stabilized lattice-oxygen participation. These findings establish threshold-controlled structure-coupled redox modulation as a cost-preserving strategy for unlocking high-energy Co-free, Ni-minimized P2-type SIB cathodes.

1. Introduction

Accelerating global environmental pollution necessitates the use of eco-friendly energy sources as well as the development of efficient energy storage systems [1–5]. While Li-ion batteries (LIBs) have been widely deployed as promising energy storage systems for both portable electronics and large-scale applications owing to their high energy density and long cycle life, concerns regarding resource concentration and long-term cost volatility of Li have intensified under rapidly growing global demand [6]. As a result, the cost competitiveness of LIBs is expected to become increasingly uncertain. These concerns have motivated extensive research into next-generation energy storage technologies with inherently lower material costs [7].

Recently, Na-ion batteries (SIBs) have emerged as strong candidates for low-cost and grid-scale energy storage systems because Na resources are naturally abundant and SIBs share a similar intercalation chemistry with LIBs [8–10]. Among various cathode classes, layered transition-metal (TM) oxides ($Na_x[TM]O_2$) have been intensively studied due to their high theoretical capacities [11,12]. In particular, to further enhance the cost competitiveness of SIBs, it is crucial to minimize the use of expensive elements such as Ni and Co in $Na_x[TM]O_2$ (targeting Ni+Co $\leq$ 0.1 mol) [13,14]. Accordingly, Co-free,

* Corresponding author at: Department of Energy Science, Sungkyunkwan University, Suwon, 16419, Republic of Korea.
E-mail address: jongsoonkim@skku.edu (J. Kim).

https://doi.org/10.1016/j.ensm.2026.105375
Received 6 May 2026; Received in revised form 14 June 2026; Accepted 8 July 2026
Available online 9 July 2026
2405-8297/© 2026 Elsevier B.V. All rights are reserved, including those for text and data mining, AI training, and similar technologies.

Ni-minimized P2-type $Na_x[Ni_aFe_bMn_c]O_2$ ($a \leq 0.1$, $a+b+c = 1$) materials possess strong potential as low-cost SIB cathodes.

Among these compositions, P2-type $Na_x[Ni_{0.1}Fe_{0.1}Mn_{0.8}]O_2$ ($x \approx 0.6$) is a representative low-cost candidate [15,16], but it suffers from limited initial charging capacity (typically below 120 mAh g^{-1}) despite delivering discharge capacities exceeding 150 mAh g^{-1}. Such a large disparity between the discharge and charge capacities severely compromises its practicality as a cathode, because the cyclable Na^+ inventory in a full cell is fixed by the Na^+ extracted during the first charge; therefore, the deliverable energy density is fundamentally limited by the initial charging capacity rather than the maximum discharge capacity [17–19]. Furthermore, insufficient Na^+ intercalation in the high-voltage region during discharge leads to a low average discharge voltage, making it difficult to realize high energy density in full-cell configurations [20]. Therefore, for practical application of Co-free, Ni-minimized ($\leq$ 0.1 mol Ni) P2-type $Na_{0.6}[Ni_{0.1}Fe_{0.1}Mn_{0.8}]O_2$ cathodes, both the initial charging capacity and the average discharge voltage must be improved.

A key factor limiting the practical applicability of these P2-type layered cathodes is their restricted Na^+ deintercalation during the initial charge, which directly constrains both the initial charging capacity and the initial Coulombic efficiency (ICE) [21]. Because this cathode relies almost exclusively on TM-based cationic redox, the amount of Na^+ that can be extracted during the first charge is inherently limited. Activation of oxygen redox provides an effective strategy to overcome this limitation by enabling additional Na^+extraction beyond the intrinsic TM redox capacity. This increases the initial charge capacity and mitigates the gap between charge and discharge capacities, thereby enabling a near-unity ICE [22–24].

In addition to enhancing Na^+ deintercalation, oxygen-redox activation also offers the potential to raise the operating voltage once the TM-based redox becomes saturated [25,26]. However, the oxidized oxygen species generated in the high-voltage region are highly reactive and tend to induce undesirable side reactions and substantial structural changes, including lattice destabilization and multiple phase transitions [27–29]. These adverse effects suppress the discharge voltage and deteriorate the rate capability, ultimately negating the benefits of accessing oxygen redox [30,31].

Therefore, achieving stable and reversible oxygen-redox activity during high-voltage cycling while simultaneously minimizing structural degradation is essential for overcoming the intrinsic voltage limitation and enabling practically meaningful energy density in Co-free, Ni-minimized P2-type Fe–Mn-based layered cathodes for low-cost and high-energy SIBs.

To meet the dual requirements of increasing the initial Na^+ extraction and raising the operating voltage, a practical cathode design for Co-free, Ni-minimized P2-type Fe–Mn-based layered cathodes must incorporate a structure-coupled redox modulator capable of (i) suppressing high-voltage structural degradation such as lattice distortion and phase evolution, (ii) stabilizing oxidized oxygen species to enable reversible oxygen-redox activity, and (iii) preserving the inherent low-cost advantage of Fe–Mn-based compositions. Such a modulator must simultaneously reinforce the lattice framework while redistributing the redox contribution beyond the intrinsic TM limit [32–35].

In this work, we show that incorporation of a redox-inactive Mg^{2+} into the P2-type Fe–Mn-based layered framework triggers threshold-governed structural coupling, leading to a reconfiguration of the redox chemistry. Specifically, once the Mg content exceeds a critical threshold, the local electronic structure and Na–O bonding environment are reorganized, inducing a transition from predominantly TM-dominated redox to cooperatively stabilized oxygen-involved redox. This transition enables Na^+ extraction beyond the intrinsic TM redox limit, thereby alleviating the inherent constraint on ICEs in P2-type Fe–Mn layered cathodes. Importantly, this strategy does not rely on increasing expensive redox-active transition metals such as Co or Ni, but instead operates via structure-coupled redox modulation triggered at a critical substitution threshold to unlock additional reversible capacity while preserving the intrinsic cost advantage of Fe–Mn-based compositions.

As a result, P2-type $Na_{0.6}[Ni_{0.1}Fe_{0.1}Mn_{0.65}Mg_{0.15}]O_2$ (P2-NFM-Mg0.15) exhibits substantially enhanced electrochemical characteristics compared to the pristine $Na_{0.6}[Ni_{0.1}Fe_{0.1}Mn_{0.8}]O_2$ (P2-NFM-Mg0). The structure-coupled redox-modulated composition increases the charge capacity, minimizes the difference between charge and discharge capacities, and elevates the average discharge voltage, indicative of stabilized high-voltage oxygen-redox participation within the P2-type layered framework. These concurrent enhancements enable more effective Na^+ inventory utilization and translate into significantly improved practical full-cell energy output.

Collectively, these findings demonstrate that structure-coupled redox modulation rather than simply increasing redox-active TM content provides a cost-preserving and mechanistically distinct pathway to maximize practical energy density in Co-free, Ni-minimized P2-type Fe–Mn-based Na-layered cathodes.

2. Material and methods

2.1. Synthesis of P2-$Na_{0.6}[Ni_{0.1}Fe_{0.1}Mn_{0.8-x}Mg_x]O_2$

P2-$Na_{0.6}[Ni_{0.1}Fe_{0.1}Mn_{0.8-x}Mg_x]O_2$ (x = 0, 0.05, 0.1, 0.113, 0.137, 0.15, 0.163, and 0.2) compounds were prepared using a solid-state method. Na_2CO_3 (Sigma-Aldrich, 99.95%), $Ni(OH)_2$ (Alfa Aesar, 96%), Fe_2O_3 (Samchun Chemical, 95%), Mn_2O_3 (Sigma-Aldrich, 99.9%), and MgO (Alfa Aesar, 99%) were used as precursors. The precursors were carefully blended at stoichiometric ratios using a high-energy ball-milling apparatus operated at 400 rpm for 12 h with silicon-nitride balls. After thorough mixing, the resulting homogeneous powder was shaped into pellets using a hydraulic press and then calcined in an O2 atmosphere at 900 °C for 12 h with a heating rate of 2.5 °C min^{-1}.

2.2. Materials characterization

The crystal structures of P2-$Na_{0.6}[Ni_{0.1}Fe_{0.1}Mn_{0.8-x}Mg_x]O_2$ (x = 0, 0.1, 0.15, and 0.2) were examined by X-ray diffraction (XRD) using a PANalytical instrument with Mo Kα radiation (wavelength = 0.70932 Å). The data were collected in the 2θ range of 4.61° to 34.32° with a 0.013° step size. Subsequently, the XRD patterns were reevaluated by converting the angles to Cu Kα radiation (wavelength = 1.54178 Å) for comparison with prior reports. The XRD refinement data were analyzed using the FullProf Rietveld program. *Operando* XRD patterns were acquired to monitor structural changes during charge/discharge at a current density of 20 mA g^{-1} within the voltage range of 2.2–4.4 V (*vs.* Na^+/Na). These *operando* XRD patterns were collected using an X-ray diffractometer (PANalytical Empyrean) equipped with Mo Kα radiation (wavelength = 0.70932 Å). The data were collected in the 2θ range of 4.0° to 35.0° with a step size of 0.013° and reevaluated by converting the angles to Cu Kα radiation (wavelength = 1.54178 Å). The elemental compositions of Na, Ni, Fe, Mn, and Mg were analyzed using inductively coupled plasma atomic emission spectroscopy (ICP-AES; OPTIMA 8300, PerkinElmer). The morphology of the materials was examined by field-emission scanning electron microscopy (FE-SEM; Gemini SEM 560, ZEISS) at 2 keV at the National Center for Inter-University Research Facilities (NCIRF), Seoul National University. Additionally, high-resolution transmission electron microscopy (HR-TEM) images and energy-dispersive X-ray spectroscopy (EDS) mappings were measured using a 200 kV scanning transmission electron microscope (JEM-ARM300F, JEOL) at the Advanced Facility Center for Quantum Technology, Sungkyunkwan University. Before the measurements, the samples were dispersed in ethanol using ultrasonication. A droplet of the suspension was then placed onto a carbon-coated copper TEM grid, and the grid was air-dried at room temperature overnight to evaporate the ethanol.

2.3. Electrochemical characterization

P2-$Na_{0.6}[Ni_{0.1}Fe_{0.1}Mn_{0.8-x}Mg_x]O_2$ (x = 0, 0.05, 0.1, 0.113, 0.137, 0.15, 0.163, and 0.2) electrodes were prepared by blending 80 wt% active material, 10 wt% Super P carbon black, and 10 wt% polyvinylidene fluoride (PVDF) with N-methyl-2-pyrrolidone (NMP) as the solvent. The resulting mixture was then coated onto aluminum foil and dried under vacuum conditions at 100 °C overnight. After drying, the electrodes were punched into disks 10 mm in diameter, and each electrode had a mass loading of approximately 3 mg cm^{-2}. For the assembly of half-cells, CR2032-type coin cells were employed. These cells included Na metal as the counter electrode, a Whatman GF/F glass-fiber separator, and an electrolyte composed of 1 M $NaPF_6$ in a solvent mixture of propylene carbonate (PC) and fluoroethylene carbonate (FEC) at a volume ratio of 98:2. The coin cells were assembled in an Ar-filled glove box. Galvanostatic charge/discharge tests were conducted at various current densities ranging from 10 to 500 mA g^{-1} in the voltage window of 2.2–4.4 V (*vs.* Na^+/Na). Battery cycling tests were performed using an automated battery charge/discharge test system (WBCS 3000, WonATech). After the initial charge/discharge cycle, cycling performance was assessed at a current density of 100 mA g^{-1}. For full-cell measurements, P2-$Na_{0.6}[Ni_{0.1}Fe_{0.1}Mn_{0.8-x}Mg_x]O_2$ cathodes were paired with hard-carbon anodes in CR2032-type coin cells. The same cathode electrodes with a mass loading of approximately 3 mg cm^{-2} were used for both half-cell and full-cell measurements. The hard-carbon anode loading was adjusted for each cathode composition to achieve an N/P ratio of 1.2 based on the half-cell capacities of the cathode and hard-carbon anode. The hard-carbon anode mass loadings were adjusted to approximately 1.5 and 1.9 mg cm^{-2} for P2-NFM-Mg0 and P2-NFM-Mg0.15 full cells, respectively. The cathode areal capacities used for electrode balancing were calculated to be 0.35 and 0.44 mAh cm^{-2} for P2-NFM-Mg0 and P2-NFM-Mg0.15, respectively, corresponding to hard-carbon anode areal capacities of 0.42 and 0.53 mAh cm^{-2}, respectively. No separate presodiation of the hard-carbon anode was performed prior to cell assembly. After assembly, the full cells were subjected to two formation cycles at a current density of 10 mA g^{-1} based on the cathode active material before subsequent electrochemical evaluation. The full cells were tested in the voltage range of 1.2–4.2 V. All full-cell capacities were calculated based on the mass of the cathode active material. P2-$Na_{0.6}[Ni_{0.1}Fe_{0.1}Mn_{0.65}Mg_{0.15}]O_2$ and P2-$Na_{0.6}[Ni_{0.1}Fe_{0.1}Mn_{0.8}]O_2$ were analyzed by ex situ X-ray absorption spectroscopy (XAS) at the Ni K-edge, Fe K-edge, and Mn K-edge. These analyses were conducted at the 8C XAFS and 7D XAFS beamlines of the Pohang Accelerator Laboratory (PAL), using Ni, Fe, and Mn metal foils as reference spectra. The XAS spectra were collected in transmission mode under high-electron-energy conditions (2.5 GeV) with a current of 200 mA, covering both the X-ray absorption near-edge structure (XANES) and extended X-ray absorption fine structure (EXAFS) regions. To investigate the valence states of O, soft X-ray absorption spectroscopy (sXAS) spectra were collected in total fluorescence yield (TFY) mode at the 4D PES beamline of PAL. The XAS data were analyzed using Athena software. The samples were prepared in the form of electrodes.

2.4. Computational details

All DFT calculations were performed using the Vienna Ab initio Simulation Package (VASP) [36]. Projector-augmented wave (PAW) pseudopotentials were used with a plane-wave basis set, as implemented in VASP [37]. The Perdew-Burke-Ernzerhof (PBE) parameterization of the generalized gradient approximation (GGA) was used for the exchange-correlation functional [38]. The GGA+U method was adopted to address d-orbital localization in Ni, Fe, and Mn ions, with U values of 6.0, 4.3, and 3.9 eV, respectively, as determined in a previous study [39]. In the DFT calculations, a 5 × 4 × 3 k-point grid was used for the 2 × 3 × 1 supercell structures of P2-$Na_{0.6}[Ni_{0.1}Fe_{0.1}Mn_{0.65}Mg_{0.15}]O_2$ and P2-$Na_{0.6}[Ni_{0.1}Fe_{0.1}Mn_{0.8}]O_2$. The Heyd-Scuseria-Ernzerhof (HSE06) hybrid functional was applied to accurately calculate the pDOS of Ni, Fe, Mn, and O ions [40]. For all calculations, the kinetic energy cutoff was set to 500 eV, and all structures were optimized until the force in the unit cell converged to within 0.03 eV $Å^{-1}$. The cluster-assisted statistical mechanics (CASM) software was used to generate Na/vacancy configurations for each composition. DFT calculations were then performed on up to 20 configurations with the lowest electrostatic energies for each composition to obtain the convex hulls of P2-$Na_{0.6}[Ni_{0.1}Fe_{0.1}Mn_{0.65}Mg_{0.15}]O_2$ and P2-$Na_{0.6}[Ni_{0.1}Fe_{0.1}Mn_{0.8}]O_2$ [41].

3. Results and discussion

3.1. Structural verification and initial electrochemical activation of fe–mn-dominant P2-Type na-layered cathodes enabling structure-coupled redox modulation

To investigate how structure-coupled redox modulation enables reversible and structurally stabilized oxygen participation in Co-free and Ni-minimized P2-type Fe–Mn-based layered cathodes, we prepared a series of compositionally controlled P2-type samples. As shown in Fig. S1 (Supporting Information), we successfully synthesized P2-$Na_{0.6}[Ni_{0.1}Fe_{0.1}Mn_{0.8-x}Mg_x]O_2$ (P2-NFM-Mg*x*, x = 0, 0.1, 0.15, and 0.2) via a conventional solid-state method, all of which exhibited a pure P2-type layered structure with the P63/mmc space group without any detectable impurities. The particle morphologies of the samples were examined using scanning electron microscopy (SEM), which revealed that all compositions exhibited similar particle shapes with particle sizes of approximately 1–2 μm (Fig. S2, Supporting Information).

For P2-NFM-Mg0.15, Rietveld refinement of the XRD pattern confirmed lattice parameters of a (= b) = 2.8953 Å and c = 11.2004 Å (Fig. 1**a**). As illustrated in Fig. 1**b**, P2-NFM-Mg0.15 crystallizes in a typical P2-type layered structure with an ABBA oxygen stacking sequence and a hexagonal framework belonging to the P63/mmc space group. The detailed crystallographic parameters, including Bisovalues, site occupancies, and atomic coordinates, are summarized in Table S1 (Supporting Information). To examine the elemental homogeneity, TEM-EDS mapping was conducted. As shown in Fig. 1**c**, all constituent elements (Na, Ni, Fe, Mn, and Mg) were uniformly distributed across the particle domains, confirming the successful incorporation of each element into the layered framework. Furthermore, the elemental ratios obtained from TEM-EDS for P2-NFM-Mg0.15 (Na: Ni: Fe: Mn: Mg = 0.6: 0.1: 0.1: 0.65: 0.15) were consistent with inductively coupled plasma atomic emission spectroscopy (ICP-AES) analysis (Fig. S3 and Table S2, Supporting Information). The P2-type layered structure was further confirmed by high-resolution transmission electron microscopy (HR-TEM), which clearly revealed well-resolved lattice fringes corresponding to the (002) planes (Fig. 1**d**). In addition, the selected-area electron diffraction (SAED) pattern exhibited distinct diffraction spots indexed to the P2 phase along the [001] zone axis (Fig. 1**e**), further verifying the well-ordered layered structure.

Fig. 1**f–i** present the first charge–discharge profiles of the representative compositions measured in half-cells. The most pronounced difference among the samples is the initial charging capacity, which increases from 117.40 mAh g^{-1} to 146.02 mAh g^{-1} as the Mg^{2+} content increases up to 0.15 mol, indicating activation of structure-coupled redox modulation, which expands Na^+ extraction beyond the intrinsic TM redox limit. A major limitation of typical P2-type Ni-minimized and Fe–Mn-based layered oxides as practical cathodes lies in their low initial charging capacity relative to the discharge capacity. In this context, the initial charge capacity and ICE should be considered together because practical cathode operation requires both sufficient Na^+ extraction during the first charge and balanced charge/discharge capacity in the first cycle. A high initial charge capacity is necessary to provide enough cyclable Na^+, while a near-unity ICE indicates that this extracted Na^+ can be effectively utilized during the subsequent discharge without a large charge/discharge mismatch. Therefore, achieving a high initial

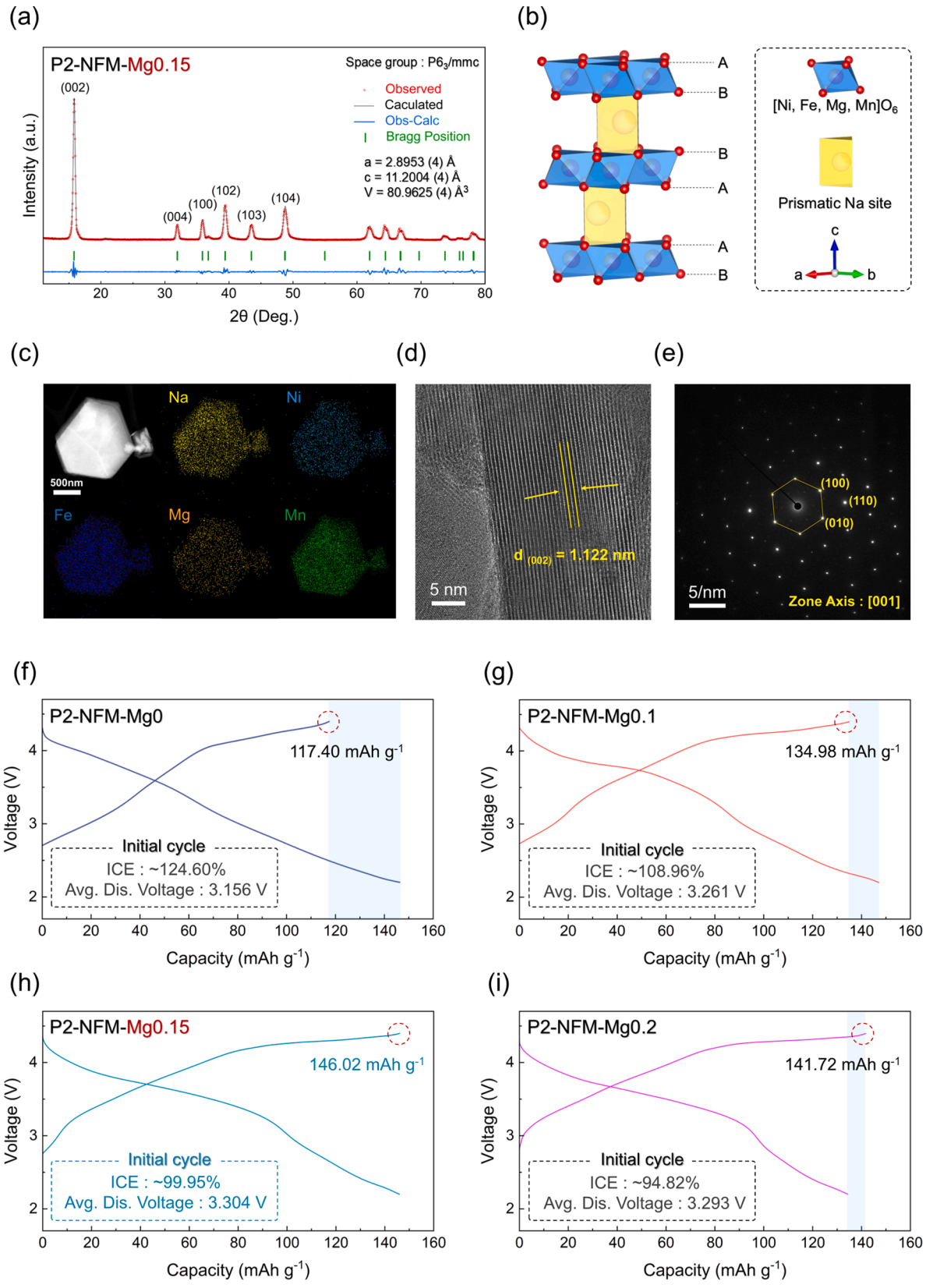

Fig. 1. (a) XRD pattern and Rietveld refinement results of P2-$Na_{0.6}[Ni_{0.1}Fe_{0.1}Mn_{0.65}Mg_{0.15}]O_2$ (R_p = 9.46%, R_{wp} = 11.8%, χ^2 = 4.40). (b) Crystal structure of P2-$Na_{0.6}[Ni_{0.1}Fe_{0.1}Mn_{0.65}Mg_{0.15}]O_2$. (c) TEM-EDS image of P2-$Na_{0.6}[Ni_{0.1}Fe_{0.1}Mn_{0.65}Mg_{0.15}]O_2$. (d) HR-TEM image of P2-$Na_{0.6}[Ni_{0.1}Fe_{0.1}Mn_{0.65}Mg_{0.15}]O_2$. (e) SAED pattern of P2-$Na_{0.6}[Ni_{0.1}Fe_{0.1}Mn_{0.65}Mg_{0.15}]O_2$. Initial charge–discharge voltage profiles of P2-$Na_{0.6}[Ni_{0.1}Fe_{0.1}Mn_{0.8-x}Mg_x]O_2$, (f) $x = 0$, (g) $x = 0.1$, (h) $x = 0.15$, and (i) $x = 0.2$.

charge capacity together with a near-unity ICE is essential for practical Na utilization. Based on this criterion, P2-NFM-Mg0 exhibits a limited initial charging capacity of 117.40 mAh g^{-1} and an ICE exceeding unity (~124.60%). This above-unity ICE does not indicate superior Na utilization; rather, it reflects a mismatch between the limited Na^+ extracted from the cathode during the first charge and the larger discharge capacity observed in the Na-metal half-cell. Because the Na-metal counter electrode can serve as an excess Na reservoir, the first discharge capacity in a half-cell does not directly represent the cyclable Na inventory available in a practical full cell. In contrast, P2-NFM-Mg0.15 delivers a higher initial charge capacity together with near-unity ICE, indicating that sufficient Na^+ can be extracted from the cathode and reversibly utilized during the subsequent discharge. This balanced first-cycle behavior provides a more practical Na inventory for full-cell operation. Notably, the average discharge voltage of P2-NFM-Mg0.15 reaches 3.304 V (*vs*. Na^+/Na), which is higher than that of P2-NFM-Mg0 (3.156 V), further contributing to its improved practical energy density.

To further resolve the compositional evolution near the proposed threshold region, the comparison was expanded by evaluating additional Mg-substituted compositions ($x = 0.05$, 0.113, 0.137, and 0.163), and their initial charge/discharge profiles are provided in Fig. S4 (Supporting Information). The Mg-content-dependent initial charge capacity and average discharge voltage are summarized in Fig. S5 (Supporting Information), where both descriptors increase at lower Mg contents and show a noticeable transition near $x = 0.15$. The near-threshold interval around $x = 0.15$ shows a more pronounced change than the lower-Mg region, supporting a threshold-like transition rather than a purely gradual compositional evolution. When the redox-inactive Mg content is further increased to 0.2 mol, both the accessible capacity and average discharge voltage begin to decline. This degradation is attributed to excessive Mg incorporation, which reduces the effective redox-active transition-metal reservoir available for charge compensation during Na^+ extraction. In addition, the first-cycle dQ/dV comparison between P2-NFM-Mg0.15 and P2-NFM-Mg0.2 (Fig. S6, Supporting Information) shows a larger voltage separation and a broader cathodic response for P2-NFM-Mg0.2, indicating increased polarization and reduced redox reversibility during Na^+ reinsertion.

These findings indicate that P2-NFM-Mg0.15 corresponds to the onset composition at which sufficient Mg substitution triggers structure-coupled redox modulation, whereas further Mg incorporation introduces an excessive-substitution effect by diluting the redox-active transition-metal reservoir and increasing discharge polarization.

3.2. *Electronic-Structure and spectroscopic evidence for oxygen-redox activation via structure-coupled redox modulation*

The electrochemical differences between P2-NFM-Mg0 and P2-NFM-Mg0.15 were further clarified through first-principles calculations. As shown in Fig. 2**a-b**, the calculated average voltage for the Na_0–$Na_{8/12}$ composition range is 3.24 V (*vs.* Na^+/Na) for P2-NFM-Mg0, whereas P2-NFM-Mg0.15 exhibits a higher calculated average voltage of 3.43 V. This calculated trend is consistent with the experimentally observed increase in average discharge voltage and supports the role of Mg substitution in modulating the redox process through structural stabilization. We attribute this voltage difference to the structure-coupled redox transition induced once the critical substitution threshold is exceeded, wherein reversible and stabilized oxygen-redox activity emerges in P2-NFM-Mg0.15, in contrast to P2-NFM-Mg0, where only TM-based cationic redox contributes to the electrochemical reaction.

To further elucidate the origin of this behavior, we analyzed the evolution of the projected density of states (pDOS) during Na^+ deintercalation in P2-NFM-Mg0.15. The full pDOS profiles of Ni, Fe, Mn, and O are provided in Fig. S7 (Supporting Information). Fig. 2**c-d** highlights the evolution of the O 2*p* states for the $Na_x[Ni_{0.1}Fe_{0.1}Mn_{0.65}Mg_{0.15}]O_2$ (Na_xNFM-Mg0.15), focusing on the changes in oxygen electronic structure near the Fermi level (E_F).

As Na^+ is deintercalated from $Na_{7/12}$NFM-Mg0.15 to $Na_{4/12}$NFM-Mg0.15, the redox activity of Ni and Fe cations is clearly observed. Notably, at the $Na_{4/12}$NFM-Mg0.15 state, a pronounced electron density appears in the O 2*p* orbital near the E_F. Upon further Na^+ deintercalation from $Na_{4/12}$NFM-Mg0.15, these electrons are depleted, and a strong O 2*p* signal emerges near E_F in the hole-density distribution of Na_0NFM-Mg0.15. This demonstrates that oxygen anions actively participate in the redox reactions at high states of charge, which contributes to the elevated average voltage of the cathode. The occurrence of these redox events was further supported by visualizing the electron and hole densities for the Na_xNFM-Mg0.15 compositions. The complete electron and hole density distributions are provided in Fig. S8 (Supporting Information). Fig. 2**e** focuses on the oxygen-related density evolution, highlighting the spatial localization associated with oxygen redox. These results confirm that Ni and Fe undergo redox first, followed by the activation of oxygen redox in the $Na_{4/12}$NFM-Mg0.15 to Na_0NFM-Mg0.15 range.

In contrast, no such oxygen-redox activity is observed in the pDOS of $Na_x[Ni_{0.1}Fe_{0.1}Mn_{0.8}]O_2$ (Na_xNFM-Mg0), as shown in Fig. S9 (Supporting Information). Across the entire Na^+ deintercalation process, P2-NFM-Mg0 exhibits only TM-based redox involving Ni, Fe, and Mn, with no contribution from O anions. This distinction indicates that once Mg substitution exceeds the critical threshold, the lattice becomes capable of stabilizing oxidized oxygen species and activating oxygen redox, thereby entering a modulated redox regime in P2-NFM-Mg0.15.

To further clarify how these local structural modifications govern anionic-redox behavior in P2-type Ni-minimized and Fe–Mn-based layered cathodes, we analyzed the redox response of oxygen anions as a function of their surrounding transition-metal coordination. Fig. S10 (Supporting Information) compares the pDOS of oxygen sites in Na_xNFM-Mg0.15 ($x = 0$ and 4/12) that exhibit distinct local bonding geometries. Oxygen atoms coordinated exclusively by Mn (*e.g.*, O10, bonded to three Mn atoms) show negligible O 2*p* intensity near E_F even at the fully charged state (Na_0), confirming minimal redox involvement. In contrast, oxygen atoms adjacent to two Mn and one heterovalent substituent (O4) exhibit a pronounced O 2*p* contribution near the E_F, indicating that the modified local environment enables active oxygen-redox participation.

These observations collectively indicate that Mg promotes oxygen-redox activity only when its substitution level exceeds the effective threshold required to reconfigure the local bonding network, confirming that structure-coupled redox modulation is a threshold-governed phenomenon rather than a linear compositional effect. While oxygen atoms coordinated only by Ni or Fe show little anionic-redox participation, those located within the reconstructed M–O–Na coordination environment formed at higher substitution levels show a marked increase in O 2*p* intensity near the Fermi level. This reinforces that the oxygen-redox activity observed in P2-NFM-Mg0.15 originates from a threshold-induced local structural coupling that does not arise at lower Mg contents.

To further substantiate the redox sequence suggested by the pDOS analysis, we analyzed the evolution of the integrated spin magnetic moments of Ni, Fe, Mn, and O as a function of Na content ($x = 7/12$, 6/12, 4/12, and 0/12) in Na_xNFM-Mg0.15 (Fig. S11, Supporting Information) [42]. The magnetic moments of Ni and Fe decrease sequentially with Na extraction, whereas the Mn moment remains nearly unchanged across the entire composition range, confirming that Mn does not participate meaningfully in the redox process. Importantly, a direct comparison of the integrated magnetic moments of oxygen anions among P2-NFM-Mg0 and P2-NFM-Mg0.15 (Fig. S12, Supporting Information) reveals a distinct increase only in P2-NFM-Mg0.15 as Na is removed from 7/12 mol to 0 mol. This pronounced rise in the O magnetic moment provides definitive evidence that oxygen redox is activated in P2-NFM-Mg0.15 during high-voltage Na^+ deintercalation, whereas P2-NFM-Mg0 shows no noticeable anionic-redox participation. The combined contributions from cationic and anionic redox processes

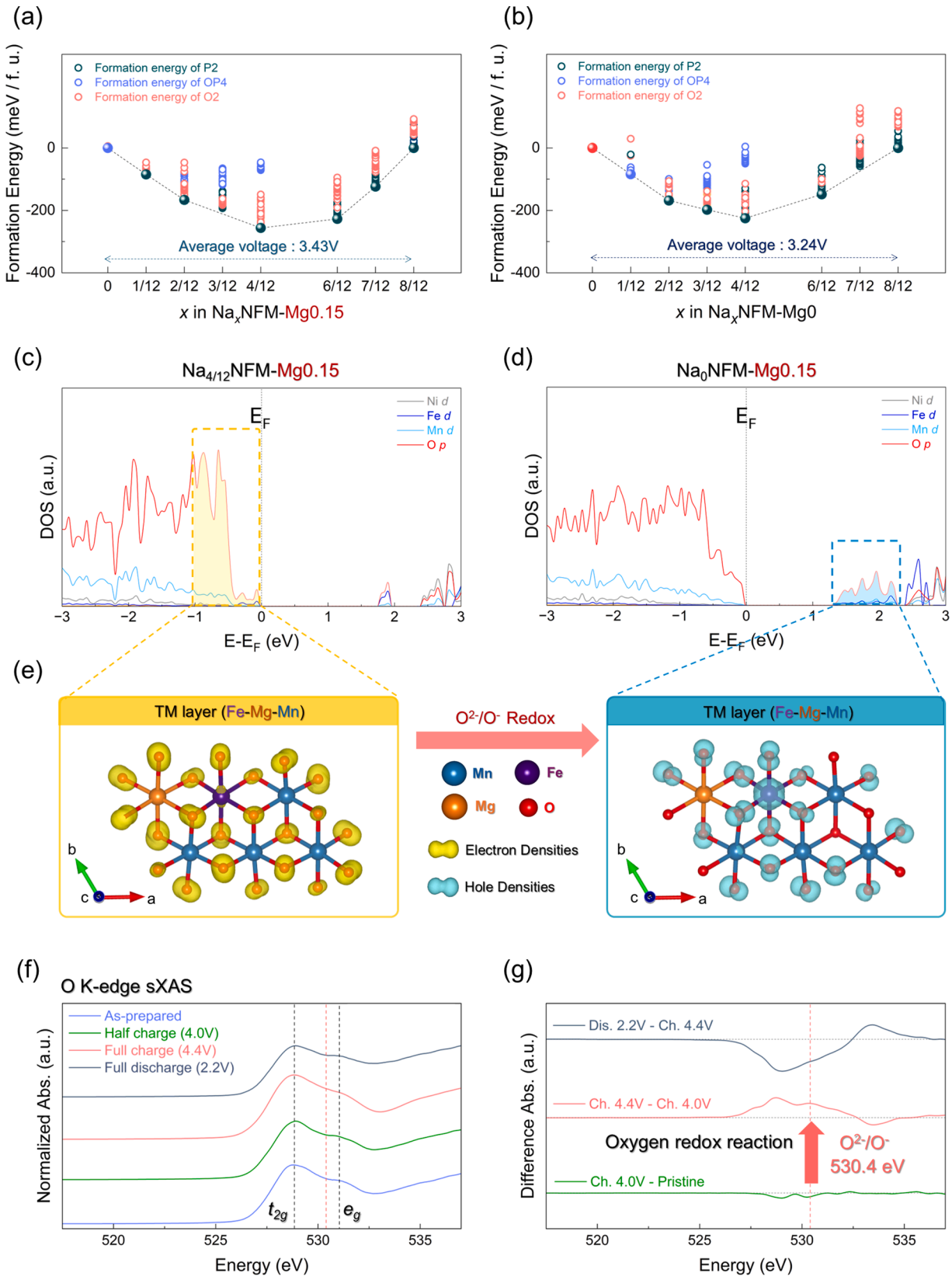

Fig. 2. Convex-hull plots of the formation energies for (a) P2-$Na_x[Ni_{0.1}Fe_{0.1}Mn_{0.65}Mg_{0.15}]O_2$ configurations ($0 \leq x \leq 8/12$) and (b) P2-$Na_x[Ni_{0.1}Fe_{0.1}Mn_{0.8}]O_2$ with the corresponding theoretical voltage profiles. Projected density of states (pDOS) of O 2*p* states in $Na_x[Ni_{0.1}Fe_{0.1}Mn_{0.65}Mg_{0.15}]O_2$: (c) $x = 4/12$ and (d) $x = 0$. (e) Visualized partial charge densities of O 2*p* states in $Na_x[Ni_{0.1}Fe_{0.1}Mn_{0.65}Mg_{0.15}]O_2$ ($x = 4/12$ and $x = 0$). (f) O K-edge sXAS spectra and (g) O K-edge difference spectra of P2-$Na_{0.6}[Ni_{0.1}Fe_{0.1}Mn_{0.65}Mg_{0.15}]O_2$.

thus account for the significantly higher average discharge voltage achieved by P2-NFM-Mg0.15, consistent with the structure-coupled redox modulation framework described above.

To provide experimental evidence for the anionic redox behavior suggested by the electronic-structure analysis, O K-edge soft X-ray absorption spectroscopy (sXAS) was performed (Fig. 2f-g). The oxygen-hole-related feature became more pronounced at the charged state and was largely recovered after discharge, supporting reversible oxygen-redox activity in P2-NFM-Mg0.15. The pre-edge feature at approximately 529 eV originates from the unoccupied TM 3*d*–O 2*p* t_{2g} hybridized states, while the e_g-related states appear near 531.4 eV. Notably, in P2-NFM-Mg0.15, a pronounced increase in spectral intensity emerges around 530.4 eV at the fully charged state. This feature is commonly associated with the formation of oxygen hole states within the O 2*p*

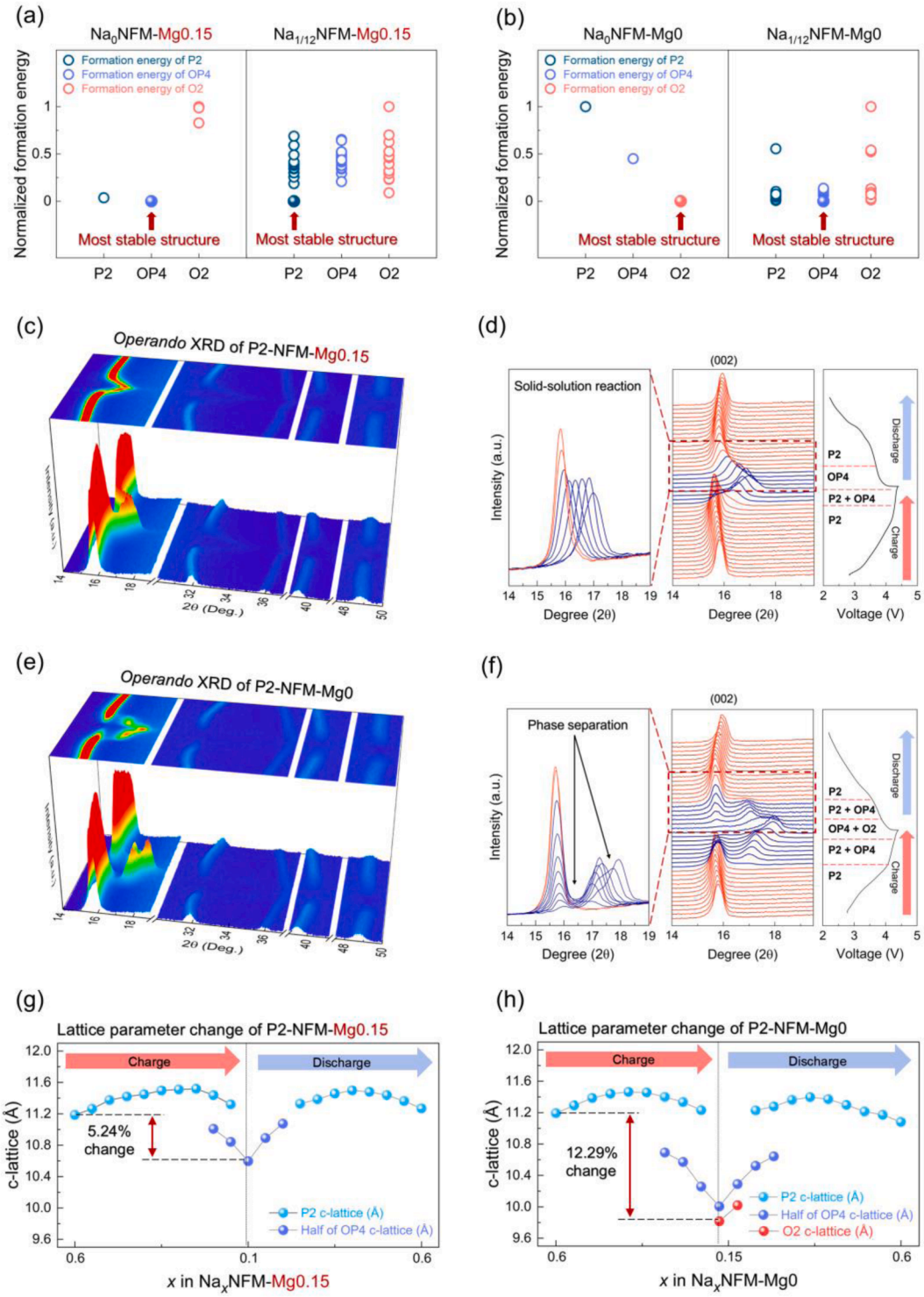

Fig. 3. Stable structures of (a) P2-$Na_x[Ni_{0.1}Fe_{0.1}Mn_{0.65}Mg_{0.15}]O_2$ and (b) P2-$Na_x[Ni_{0.1}Fe_{0.1}Mn_{0.8}]O_2$ at $x = 0$ and 1/12. (c) *Operando* XRD patterns and (d) voltage profile with magnified *operando* XRD patterns of P2-$Na_{0.6}[Ni_{0.1}Fe_{0.1}Mn_{0.65}Mg_{0.15}]O_2$ during charge/discharge. (e) *Operando* XRD patterns and (f) voltage profile with magnified *operando* XRD patterns of P2-$Na_{0.6}[Ni_{0.1}Fe_{0.1}Mn_{0.8}]O_2$ during charge/discharge. Changes in *c*-axis lattice parameters of (g) $Na_x[Ni_{0.1}Fe_{0.1}Mn_{0.65}Mg_{0.15}]O_2$ and (h) $Na_x[Ni_{0.1}Fe_{0.1}Mn_{0.8}]O_2$ during charge/discharge.

band, indicating the involvement of lattice oxygen in the charge compensation process. Differential electrochemical mass spectrometry (DEMS) during the initial charge further showed no noticeable O_2 or CO_2 evolution up to 4.4 V (Fig. S13, Supporting Information), excluding measurable gas-generating side reactions and supporting reversible lattice oxygen redox as the main origin of the high-voltage capacity. These combined sXAS and DEMS results provide direct experimental evidence for oxygen-redox participation at high states of charge without noticeable oxygen release or severe electrolyte decomposition.

These computational and experimental results establish a coherent mechanistic picture of the redox chemistry in Fe–Mn-dominant P2-type cathodes. When the Mg content remains below the critical threshold, charge compensation proceeds primarily through conventional TM-based cationic redox. Once the substitution level exceeds the threshold required to modify the local bonding environment, however, a structure-coupled redox transition emerges. This transition stabilizes oxidized oxygen species and enables the participation of lattice oxygen in the charge-compensation process. As a result, the redox chemistry evolves from a purely TM-dominated regime to a cooperative cationic-anionic redox mechanism. The threshold-enabled oxygen-redox contribution, together with the stabilized structural framework, increases the accessible Na^+ extraction and raises the average operating voltage, thereby providing a mechanistic basis for the enhanced electrochemical performance of P2-NFM-Mg0.15.

3.3. Suppressed high-voltage phase evolution enabled by structure-coupled redox modulation

Beyond the voltage enhancement discussed above, first-principles calculations further clarify why P2-NFM-Mg0.15 is able to extract a larger amount of Na during the initial charge than P2-NFM-Mg0 [43,44]. In P2-type layered cathodes, high-voltage charging typically triggers a sequence of structural transitions—from P2 to OP4 to O2—each accompanied by substantial lattice distortion. Such structural transitions impose a significant energetic penalty that limits the accessible Na extraction and leads to large overpotentials [45,46].

As shown in Fig. 3a-b, the predicted stable structures at highly desodiated states indicate that structure-coupled redox modulation stabilizes the P2 framework and suppresses detrimental high-voltage phase evolution. This structural stabilization explains why P2-NFM-Mg0.15 is capable of extracting a larger amount of Na during the initial charge compared with P2-NFM-Mg0.

To experimentally verify these predictions, *operando* X-ray diffraction measurements were performed during electrochemical cycling. In P2-NFM-Mg0.15 (Fig. 3c-d), the P2 phase is retained up to 4.2 V and then evolves smoothly into the OP4 phase. Notably, the discharge process involves a direct OP4 → P2 transition without any discernible phase separation, as evidenced by the continuous peak shift, which is characteristic of solid-solution-like structural evolution. By contrast, P2-NFM-Mg0 (Fig. 3e-f) exhibits a well-defined P2 → OP4 transition around 4.0 V, followed by the emergence of an O2 phase above 4.2 V. Clear phase separation is observed, as shown by the appearance of a distinct diffraction peak near 17° To clarify whether this stabilized structural pathway emerges at a specific Mg-substitution level, Mg-content-dependent *operando* XRD patterns were further compared for representative compositions (Fig. S14, Supporting Information). P2-NFM-Mg0.1 still exhibits phase-separated high-voltage evolution similar to P2-NFM-Mg0, whereas P2-NFM-Mg0.15 and P2-NFM-Mg0.2 show solid-solution-like structural evolution with suppressed phase separation. This comparison indicates that the structural reaction pathway changes from phase-separated to solid-solution-like behavior near $x = 0.15$. The retention of the solid-solution-like pathway in P2-NFM-Mg0.2, despite its slightly lower capacity, further suggests that $x = 0.15$ corresponds to the onset of the stabilized structural regime rather than merely the composition with optimal electrochemical performance.

The lattice evolution during cycling further supports this structural transition. Because the OP4 phase has an approximately doubled *c*-axis length compared with the P2 and O2 phases, the OP4 lattice parameters were normalized using $c/2$ and $V/2$ for comparison of the c-axis and unit-cell volume evolution. Based on this normalized comparison, P2-NFM-Mg0.15 exhibits a much smaller *c*-axis variation of 5.24% than P2-NFM-Mg0, which shows a *c*-axis variation of 12.29% (Fig. 3g-h). This confirms that the solid-solution-like pathway effectively mitigates the interlayer-distance fluctuation during high-voltage Na^+ extraction/insertion. Additional analyses of the *a*-axis variation and unit-cell volume evolution during charge/discharge also show smaller changes in P2-NFM-Mg0.15 than in P2-NFM-Mg0 (Fig. S15 and Fig. S16, Supporting Information). This reduced structural distortion indicates that P2-NFM-Mg0.15 maintains far greater structural integrity during high-voltage cycling, which contributes to its higher average discharge voltage, practical energy density, and enhanced cycling stability.

3.4. Suppressed voltage decay and enhanced practical energy density enabled by structure-coupled redox modulation

The enhanced structural stability directly translates into improved long-term cycling performance. As shown in Fig. 4**a**, P2-NFM-Mg0.15 maintains the high capacity retention of ~71.50% after 200 cycles at 100 mA g^{-1}, whereas P2-NFM-Mg0 retains only ~48.08% under the same conditions. In addition, long-term half-cell cycling at 500 mA g^{-1} further confirmed the superior high-rate durability of P2-NFM-Mg0.15, which retained 70.45% of its initial capacity after 200 cycles compared with 41.67% for P2-NFM-Mg0 (Fig. S17, Supporting Information). Notably, the disparity becomes even more pronounced when comparing the practical energy density (Fig. 4**b**), which reflects not only the capacity but also the operating voltage. This clearly indicates that the higher and more stable average discharge voltage of P2-NFM-Mg0.15 is sustained throughout prolonged cycling, unlike in P2-NFM-Mg0.

As shown in Fig. 4c, P2-NFM-Mg0 exhibits an already low initial average discharge voltage of 3.08 V in the first cycle, which further declines to 2.61 V by the 200th cycle. In stark contrast, P2-NFM-Mg0.15 begins at a higher value of 3.18 V and maintains 2.94 V even after 200 cycles. The voltage decay behavior is further elucidated through dQ/dV analysis. P2-NFM-Mg0.15 retains both the shape and the positions of its major dQ/dV features with only minimal shifts, indicating highly stable and reversible redox reactions during extended cycling (Fig. 4d). In contrast, P2-NFM-Mg0 exhibits pronounced peak shifts and a substantial loss of peak definition after 200 cycles (Fig. 4e), reflecting progressive degradation of the reaction pathways despite relying solely on TM-based redox reactions.

To further assess whether the oxygen-involved redox remains reversible after long-term cycling, post-cycling O K-edge sXAS was performed for P2-NFM-Mg0.15 after 200 cycles (Fig. S18, Supporting Information). The oxygen-hole-related feature at ~530.4 eV is clearly observed at the fully charged state and is largely reduced after full discharge, indicating reversible formation and recovery of oxygen-hole states even after prolonged cycling. This result confirms that the oxygen-redox process remains operative and largely reversible in the stabilized P2-NFM-Mg0.15 framework, consistent with the well-preserved dQ/dV features and suppressed voltage decay.

Building upon the stabilized redox behavior observed in half-cell configurations, we further evaluated the practical applicability of the modulated P2-type Fe–Mn-based layered cathode in full-cell systems paired with a hard-carbon (HC) anode under capacity-balanced conditions. As shown in Fig. 4f, the P2-NFM-Mg0.15||HC full cell delivers a reversible discharge capacity of ~132.87 mAh g^{-1}, significantly exceeding that of the non-modulated counterpart (~111.54 mAh g^{-1}). This enhancement directly reflects improved initial Na extraction and more efficient cyclable Na utilization arising from the reconfigured redox pathway.

Long-term cycling further highlights the stability of the engineered redox regime. The P2-NFM-Mg0.15||HC full cell retains ~82.25% of its

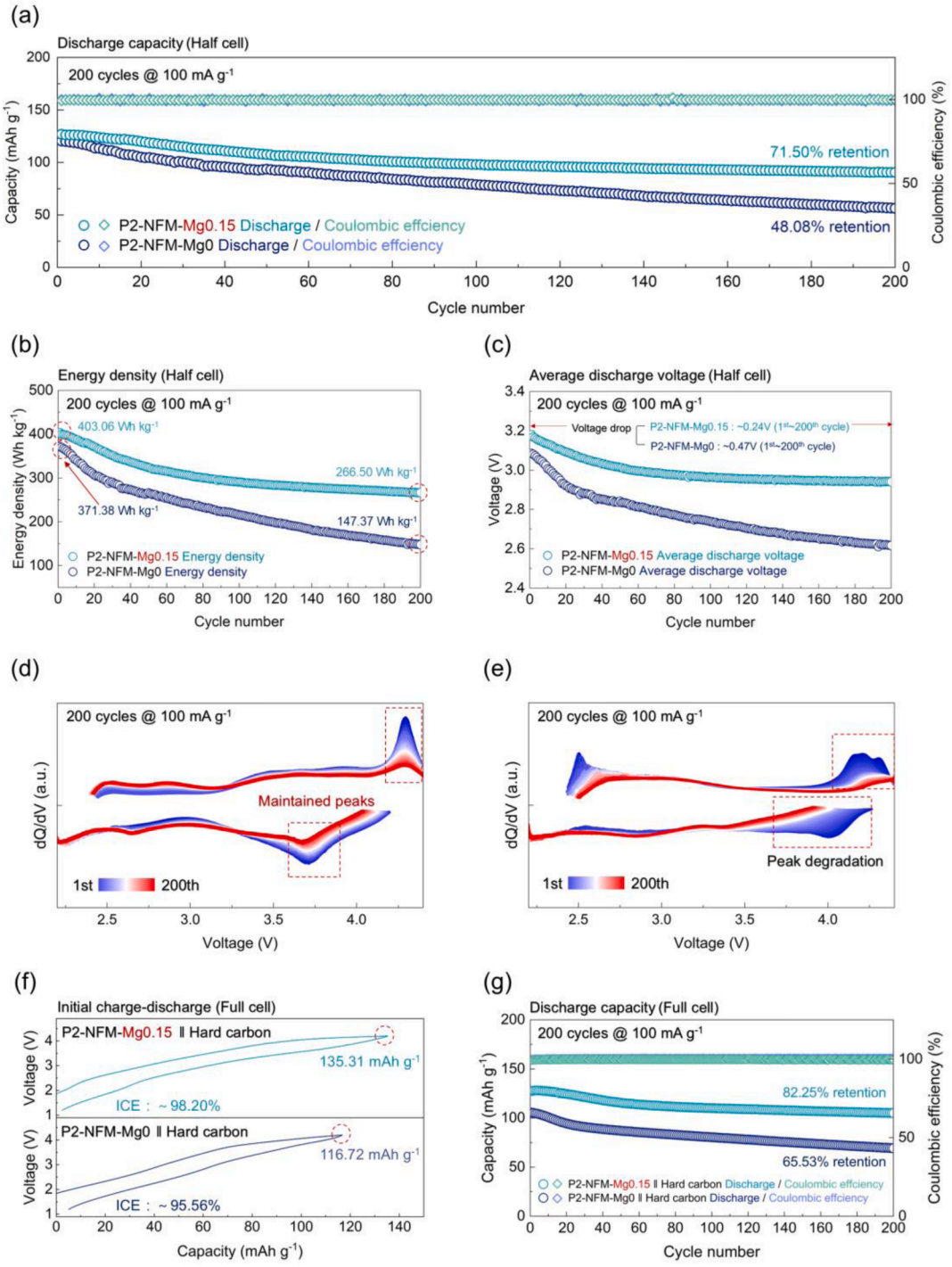

Fig. 4. Comparison of the (a) discharge capacity, (b) energy density, and (c) average discharge voltage of P2-$Na_{0.6}[Ni_{0.1}Fe_{0.1}Mn_{0.65}Mg_{0.15}]O_2$ and P2-$Na_{0.6}[Ni_{0.1}Fe_{0.1}Mn_{0.8}]O_2$ measured over 200 cycles at a current density of 100 mA g^{-1}. dQ/dV profiles of (d) P2-$Na_{0.6}[Ni_{0.1}Fe_{0.1}Mn_{0.65}Mg_{0.15}]O_2$ and (e) P2-$Na_{0.6}[Ni_{0.1}Fe_{0.1}Mn_{0.8}]O_2$ during 200 cycles at 100 mA g^{-1} in the voltage range of 2.2–4.4 V. (f) Initial charge–discharge voltage profiles of the corresponding full cells measured in the voltage range of 1.2–4.2 V. (g) Discharge capacity and Coulombic efficiency of the full cells measured over 200 cycles at 100 mA g^{-1} in the voltage range of 1.2–4.2 V.

initial capacity after 200 cycles, whereas the non-modulated system maintains only ~65.53% under identical conditions (Fig. 4g). Notably, the engineered system exhibits minimal polarization growth and sustained discharge voltage profiles throughout cycling, while the counterpart without structure-coupled redox modulation suffers from progressive voltage decay and increased overpotential (Fig. S19, Supporting Information). These results confirm that structure-coupled redox modulation not only enhances intrinsic cathode electrochemistry but also translates directly into superior practical energy density and cycling stability at the full-cell level.

The superior cycling stability of P2-NFM-Mg0.15 is further corroborated by post-cycling morphological and structural analyses. Ex situ SEM observations reveal that P2-NFM-Mg0 particles develop extensive intragranular cracks after 100 cycles (Fig. S20, Supporting Information), indicative of severe mechanical degradation accumulated through repeated lattice mismatch during the P2–OP4–O2 transitions. In

contrast, P2-NFM-Mg0.15 particles retain clean surfaces with no visible cracking, suggesting a substantial reduction in mechanical degradation.

Ex situ XRD analysis after cycling provides additional confirmation of these structural differences. For P2-NFM-Mg0 (Fig. S21, Supporting Information), the characteristic diffraction peaks show clear signs of degradation accompanied by a noticeable shift of the (002) reflection to higher 2θ, indicative of interlayer contraction and irreversible structural distortion. P2-NFM-Mg0.15 (Fig. S22, Supporting Information), however, exhibits only minimal peak broadening and virtually no shift in the (002) peak, demonstrating excellent structural retention throughout prolonged cycling. These results collectively demonstrate that structure-coupled redox modulation stabilizes both the redox chemistry and the lattice framework of Fe–Mn-dominant P2-type cathodes. By suppressing high-voltage phase evolution and mitigating lattice distortion, the engineered system effectively prevents voltage decay and enables sustained high-voltage operation during prolonged cycling.

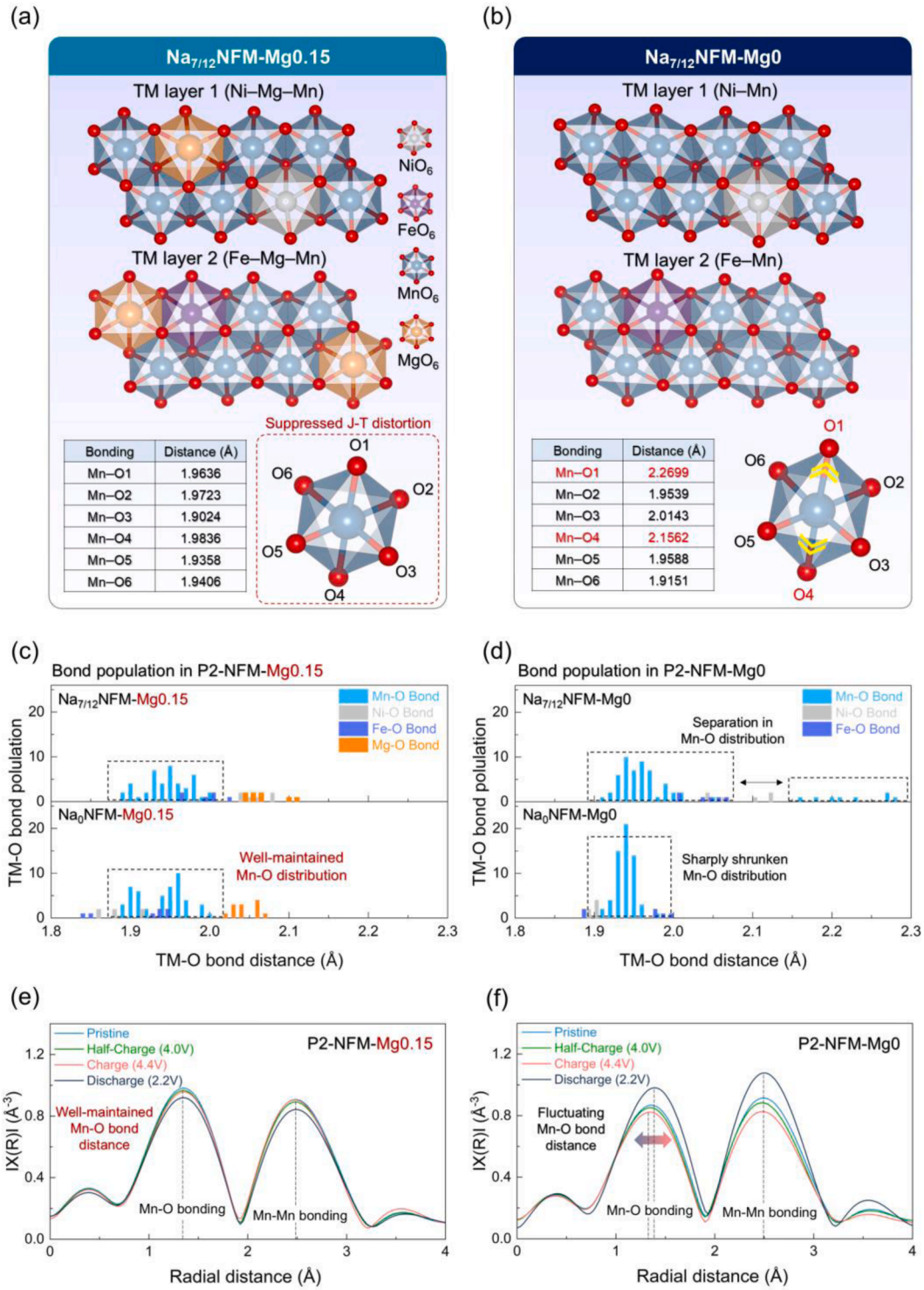

Fig. 5. Comparison of predicted Mn–O bond distances in MnO_6 octahedra between (a) P2-$Na_x[Ni_{0.1}Fe_{0.1}Mn_{0.65}Mg_{0.15}]O_2$ and (b) P2-$Na_x[Ni_{0.1}Fe_{0.1}Mn_{0.8}]O_2$ ($x = 7/12$). Comparison of transition-metal-oxygen (TM–O) bond-length distributions in (c) P2-$Na_x[Ni_{0.1}Fe_{0.1}Mn_{0.65}Mg_{0.15}]O_2$ and (d) P2-$Na_x[Ni_{0.1}Fe_{0.1}Mn_{0.8}]O_2$. Mn K-edge EXAFS analyses of various charge/discharge states of (e) P2-$Na_{0.6}[Ni_{0.1}Fe_{0.1}Mn_{0.65}Mg_{0.15}]O_2$ and (f) P2-$Na_{0.6}[Ni_{0.1}Fe_{0.1}Mn_{0.8}]O_2$.

3.5. Local lattice stabilization and suppressed Jahn–teller distortion via structure-coupled redox modulation

While the suppression of slab gliding and high-voltage phase evolution is essential for maintaining global structural integrity, local lattice distortions within the TM–O framework can also critically affect cycling stability. To clarify the local origin of this stabilization, we examined the evolution of MnO_6 octahedra and TM–O bond environments, with particular focus on the structural-buffering role of redox-inactive Mg^{2+} within the TM layer. First-principles calculations were performed to examine the evolution of MnO_6 octahedra in Na_xNFM-Mg0.15 and Na_xNFM-Mg0 at two representative Na contents ($x = 7/12$ and $x = 0$) (Fig. 5a-b and Fig. S23, Supporting Information). In $Na_{7/12}$NFM-Mg0, the MnO_6 octahedra displayed a pronounced Jahn–Teller distortion, characterized by significant elongation of specific Mn–O bonds, with Mn–O1 and Mn–O4 bond lengths extending to approximately 2.27 Å and 2.16 Å, respectively. These lengths are considerably longer than the other Mn–O bonds, demonstrating an uneven and distorted octahedral environment. Upon full Na extraction ($x = 0$), these elongated bonds contracted to ~1.93 Å, approaching the lengths of the remaining Mn–O bonds. Although partially reversible, this bond-length evolution indicates persistent local instability during cycling.

In contrast, $Na_{7/12}$NFM-Mg0.15 exhibited no significant distortion in the MnO_6 octahedra, with Mn–O bond lengths remaining uniform and evenly distributed. This uniformity demonstrates that once the Mg^{2+} content surpasses the effective substitution threshold ($\geq$ 0.15 mol), the Jahn–Teller distortion associated with Mn^{3+} is effectively suppressed. Such suppression contributes to enhanced local structural stability and greater lattice flexibility during Na^+ de/intercalation in P2-NFM-Mg0.15, further stabilizing the modulated redox regime across the full voltage window.

To further quantify the local structural environment, the overall TM–O bond-length distribution was analyzed during Na^+ de/intercalation (Fig. 5c-d). P2-NFM-Mg0.15 maintains a narrow and well-defined bond-length distribution throughout cycling, indicating high configurational uniformity and enhanced structural flexibility within the TM–O framework. In contrast, P2-NFM-Mg0 exhibits a broader and more fluctuating TM–O bond distribution, consistent with the Jahn–Teller distortion associated with Mn^{3+} and the resulting structural instability.

These computational results are strongly supported by synchrotron-based X-ray absorption spectroscopy analyses. In the Mn K-edge XANES spectra of P2-NFM-Mg0.15, negligible edge shifts are observed during charge and discharge (Fig. S24a, Supporting Information), indicating that Mn remains predominantly in the Mn^{4+} state and does not participate in the electrochemical redox process. By contrast, P2-NFM-Mg0 exhibits pronounced Mn K-edge shifts during charge with full recovery upon discharge (Fig. S24b, Supporting Information), confirming the occurrence of Mn^{3+}/Mn^{4+} redox reactions. Because Mn^{3+} induces lattice distortions due to its electronic configuration, this redox activity directly drives the Jahn–Teller distortion observed in P2-NFM-Mg0. In addition, ex situ XANES analyses of the Ni and Fe K-edges (Fig. S25, Supporting Information) confirm that Ni and Fe ions participate in the redox reactions in P2-NFM-Mg0.15, consistent with the first-principles predictions.

To further probe the dynamic structural behavior during cycling, ex situ EXAFS analyses were performed (Fig. 5**e-f**). The results reveal that in P2-NFM-Mg0, the Mn–O bond length increased during discharge and decreased during charge, indicating the presence of Mn^{3+}-induced Jahn–Teller distortion. In contrast, P2-NFM-Mg0.15 exhibited nearly stable Mn–O bond lengths throughout cycling, demonstrating the effective suppression of local lattice distortions, consistent with the computational results.

Collectively, these results demonstrate that redox-inactive Mg^{2+} serves as a structural buffer within the TM layer, stabilizing the MnO_6 octahedral environment and narrowing the TM–O bond-length distribution during Na^+ de/intercalation. Importantly, this geometric buffering acts beyond the conventional Mn-valence effect: in addition to reducing the Jahn–Teller-active Mn^{3+} fraction through the increased average Mn valence, the redox-inactive Mg^{2+} further buffers the residual Mn^{3+}-associated Jahn–Teller distortion through a valence-independent, geometric stabilization of the local lattice. Consequently, the local lattice distortion in P2-NFM-Mg0.15 is suppressed by these two cooperative but mechanistically distinct contributions, rather than being explained solely by conventional Mn-valence regulation. Together with the previously demonstrated suppression of high-voltage phase transitions, this stabilization of both the local and global lattice structures provides a mechanistic basis for the superior structural robustness and improved cycling performance of P2-NFM-Mg0.15.

This local lattice stabilization should be distinguished from the high-voltage oxygen-redox contribution discussed above. The Mn-valence regulation and Mg^{2+}-buffering effects mainly suppress Mn^{3+}-associated Jahn–Teller distortion and stabilize the local TM–O framework, whereas the additional high-voltage capacity and voltage enhancement are associated with threshold-enabled oxygen-redox participation, which is observed in P2-NFM-Mg0.15 but absent in P2-NFM-Mg0. Therefore, the enhanced performance of P2-NFM-Mg0.15 arises from the coupling of Mn^{3+}-related local distortion suppression, redox-inactive Mg^{2+}-buffered lattice stabilization, high-voltage phase-evolution suppression, and threshold-enabled oxygen-redox participation.

3.6. Enhanced Na^+diffusion kinetics and rate capability enabled by structure-coupled redox modulation

Building on the improved structural durability described above, P2-NFM-Mg0.15 also exhibits significantly improved rate capability. As shown in Fig. 6a-b, P2-NFM-Mg0.15 and P2-NFM-Mg0 exhibited comparable discharge capacities of 145.28 mAh g^{-1} and 145.59 mAh g^{-1}, respectively, at a low current density of 10 mA g^{-1}. However, at a higher rate of 500 mA g^{-1}, P2-NFM-Mg0.15 exhibited a significantly higher capacity of 118.17 mAh g^{-1} compared to 105.20 mAh g^{-1} for P2-NFM-Mg0.

We additionally calculated the average discharge voltages at each current density. Across all tested rates, P2-NFM-Mg0.15 consistently exhibited higher average discharge voltages than P2-NFM-Mg0, indicating its superior voltage retention under both low- and high-rate conditions (Fig. 6c). To further assess the high-voltage stability under rate variation, we compared the discharge voltages measured at 10 mA g^{-1} and 500 mA g^{-1} at a comparable discharge capacity of ~10 mAh g^{-1} (Fig. S26, Supporting Information). P2-NFM-Mg0.15 exhibited a smaller voltage difference of 0.56 V, whereas P2-NFM-Mg0 showed a larger difference of 0.70 V, confirming the smaller voltage drop in P2-NFM-Mg0.15 under high-rate conditions. While oxygen redox activity is generally associated with slower kinetics and a pronounced voltage drop at high rates, P2-NFM-Mg0.15 demonstrated a relatively suppressed voltage drop. This superior performance can be attributed to the enhanced structural stability at high voltages, as discussed previously, which effectively mitigates the typical voltage decline associated with oxygen redox under high-rate conditions. Notably, the Ragone plot (Fig. 6d) further highlights the superior power capability of P2-NFM-Mg0.15 compared with previously reported P2- and O3-type layered oxide cathodes for SIBs [47–53]. To provide a more compositionally and mechanistically relevant benchmark, representative Mg-substituted and oxygen-redox-based P2/P3 layered cathodes were additionally compared in Table S3 (Supporting Information) [54–57].

To further clarify the kinetic origin of this improved rate capability, additional GITT, scan-rate-dependent CV, and EIS analyses were conducted [58–62]. The GITT results show that P2-NFM-Mg0.15 maintains higher apparent Na^+ diffusion coefficients than P2-NFM-Mg0 over the charge/discharge region (Fig. S27, Supporting Information), indicating facilitated Na^+ transport during Na^+ extraction and insertion. Consistently, the scan-rate-dependent CV analysis shows a linear $|i_p|$ *vs.* $v^{1/2}$ relationship, indicating a predominantly diffusion-controlled process,

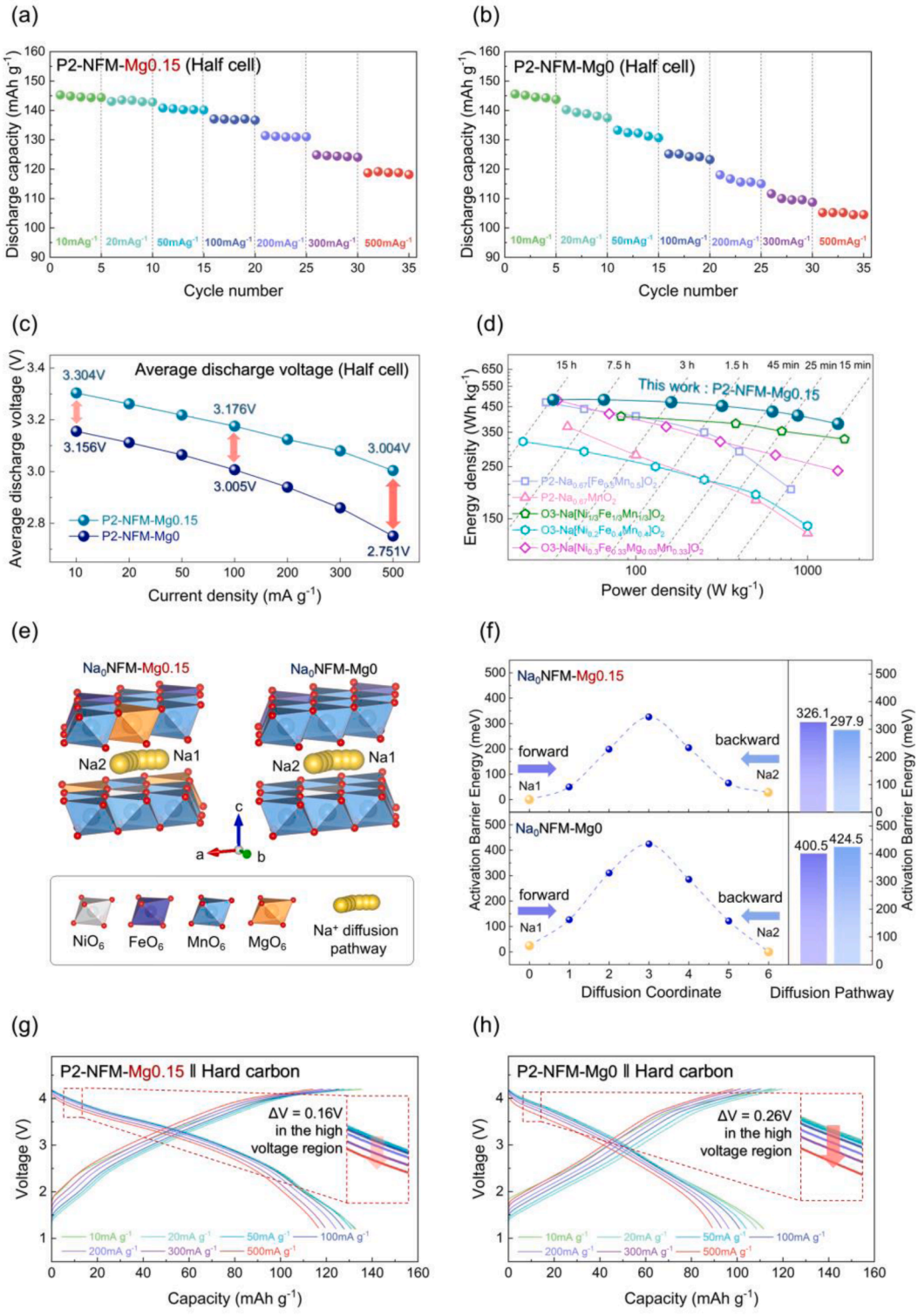

Fig. 6. Rate-capability of (a) P2-$Na_{0.6}[Ni_{0.1}Fe_{0.1}Mn_{0.65}Mg_{0.15}]O_2$ and (b) P2-$Na_{0.6}[Ni_{0.1}Fe_{0.1}Mn_{0.8}]O_2$ half cells at various current densities in the voltage range of 2.2–4.4 V (*vs.* Na^+/Na). (c) Rate-dependent average discharge voltages of P2-$Na_{0.6}[Ni_{0.1}Fe_{0.1}Mn_{0.65}Mg_{0.15}]O_2$ and P2-$Na_{0.6}[Ni_{0.1}Fe_{0.1}Mn_{0.8}]O_2$ half cells. (d) Comparison of energy and power densities among P2-$Na_{0.6}[Ni_{0.1}Fe_{0.1}Mn_{0.65}Mg_{0.15}]O_2$ and other reported layered oxide cathodes for SIBs. (e) Predicted Na^+ diffusion pathway in P2-$Na_{0.6}[Ni_{0.1}Fe_{0.1}Mn_{0.65}Mg_{0.15}]O_2$ and P2-$Na_{0.6}[Ni_{0.1}Fe_{0.1}Mn_{0.8}]O_2$ and (f) predicted activation barrier energy for Na^+ diffusion. Galvanostatic charge–discharge profiles of (g) P2-$Na_{0.6}[Ni_{0.1}Fe_{0.1}Mn_{0.65}Mg_{0.15}]O_2$ ‖ Hard carbon and (h) P2-$Na_{0.6}[Ni_{0.1}Fe_{0.1}Mn_{0.8}]O_2$ ‖ Hard carbon full cells at various current densities (10, 20, 50, 100, 200, 300, and 500 mA g^{-1}) in the voltage range of 1.2–4.2 V.

with larger slopes for P2-NFM-Mg0.15 than for P2-NFM-Mg0 (Fig. S28, Supporting Information), further supporting faster diffusion-controlled Na^+ storage kinetics. In addition, EIS results show a smaller semicircle for P2-NFM-Mg0.15 than for P2-NFM-Mg0 (Fig. S29, Supporting Information), corresponding to a lower charge-transfer resistance (R_{ct}) and indicating more facile interfacial charge transfer. These experimental results collectively demonstrate that P2-NFM-Mg0.15 enables more facile Na^+ extraction/insertion kinetics than P2-NFM-Mg0.

The enhanced kinetics of P2-NFM-Mg0.15 were also verified through a comprehensive theoretical analysis of Na^+ diffusion pathways and activation barriers in both compositions. Based on nudged elastic band (NEB) calculations using first-principles methods (Fig. 6e-f), the Na^+ diffusion barrier in P2-NFM-Mg0.15 (~311.99 meV) is significantly lower than that in P2-NFM-Mg0 (~412.53 meV), underscoring the improved Na^+ diffusion kinetics and power capability of P2-NFM-Mg0.15.

A similar trend was also observed in practical full-cell configurations. As shown in Fig. 6**g-h**, the P2-NFM-Mg0.15||HC cell exhibited improved rate capability and a smaller voltage drop at high current densities compared with the P2-NFM-Mg0||HC counterpart, consistent with the half-cell results. These results further highlight that the Mg-modulated structure effectively suppresses rate-induced polarization not only in the half-cell measurements but also in practical cell configurations.

Overall, these results confirm that structure-coupled redox modulation, once activated beyond the substitution threshold, synergistically stabilizes oxygen redox, suppresses high-voltage phase evolution, mitigates Jahn–Teller distortion, and enhances Na^+ diffusion kinetics. This integrated stabilization enables a rare combination of high energy density, excellent rate capability, and long-term cycling stability in Fe–Mn-dominant P2-type cathodes.

4. Conclusion

In this work, we identified the intrinsic TM redox limitation as the fundamental bottleneck restricting practical energy density in Co-free, Ni-minimized P2-type Fe–Mn-based layered cathodes. By activating structure-coupled redox modulation beyond a critical substitution threshold (0.15 mol Mg), we reconfigured the redox pathway from purely TM-dominated behavior to cooperatively stabilized oxygen-involved redox, thereby expanding the accessible Na^+ extraction window without compromising structural integrity. As a direct consequence, the optimized composition delivered a substantial increase in initial charging capacity (117.40 → 146.02 mAh g^{-1}), a near-unity ICE (~124.60% → ~99.95%), and a pronounced elevation in average discharge voltage (3.156 → 3.304 V), collectively resulting in significantly enhanced practical energy density. In full-cell configurations paired with hard carbon, the modulated cathode delivered a reversible discharge capacity of ~132.87 mAh g^{-1} (*vs.* ~111.54 mAh g^{-1} for the non-modulated counterpart) and retained ~82.25% of its initial capacity after 200 cycles, markedly outperforming the ~65.53% retention of the non-modulated system under identical conditions. Importantly, *operando* structural analysis revealed that the lattice-parameter variation along the *c*-axis was substantially reduced from 12.29% in P2-NFM-Mg0 to 5.24% in P2-NFM-Mg0.15, demonstrating markedly suppressed high-voltage structural distortion. This reduced lattice change during charge/discharge confirms that structure-coupled redox modulation stabilizes both global phase evolution and local octahedral environments during Na^+ de/intercalation. Although demonstrated here with Mg^{2+}, the threshold-governed, structure-coupled redox modulation may provide a broader design concept for using redox-inactive or low-valent cations to couple oxygen-redox activation with structural stabilization. However, extending this concept to other dopants, such as Zn^{2+} or Li^+, would require dopant-specific optimization because the critical composition and extent of redox/structural modulation are expected to depend on ionic radius, charge, site preference, solubility limit, and host-composition-dependent phase stability. Overall, this work establishes structure-coupled redox modulation as a threshold-triggered design principle—rather than a linear compositional effect—providing a cost-preserving and mechanistically validated pathway to unlock low-cost, high-energy Co-free, Ni-minimized P2-type layered cathodes for SIBs.

CRediT authorship contribution statement

Sunghyun Lim: Validation, Investigation, Formal analysis. **Jeongwoo Kim:** Writing – original draft, Visualization, Validation, Formal analysis. **Bonyoung Ku:** Methodology, Investigation. **Myungeun Choi:** Methodology, Investigation. **Hoseok Lee:** Visualization, Methodology. **Junha Kwon:** Validation, Methodology. **Lahyeon Jang:** Investigation, Formal analysis. **Taegyu Kim:** Validation, Investigation. **Hun-Gi Jung:** Supervision, Project administration. **Junyoung Mun:** Supervision, Data curation. **Jongsoon Kim:** Writing – review & editing, Visualization, Supervision, Project administration, Funding acquisition, Formal analysis, Data curation, Conceptualization.

Declaration of competing interest

The authors declare that they have no known competing financial interests or personal relationships that could have appeared to influence the work reported in this paper.

Acknowledgements

This research was supported by a grant from the National Research Council of Science & Technology (NST), funded by the Korea Government (MSIT) (No. GTL24012-000). This work was also supported by the Technology Innovation Program (RS-2024-00403571, Development of High-Capacity Layered Oxide Cathode Material for Sodium-Ion Batteries) funded by the Ministry of Trade, Industry and Energy (MOTIE, Korea). In addition, this work was supported by the Korea Institute for Advancement of Technology (KIAT) grant funded by the Korea Government (MOTIE) (No. RS-2025-02073015, HRD Program for Industrial Innovation).

Supplementary materials

Supplementary material associated with this article can be found, in the online version, at doi:10.1016/j.ensm.2026.105375.

Data availability

Data will be made available on request.

References

[1] Q. Meng, Y. Huang, L. Li, F. Wu, R. Chen, Smart batteries for powering the future, Joule 8 (2024) 344–373, https://doi.org/10.1016/j.joule.2024.01.011.
[2] F. Degen, M. Winter, D. Bendig, J. Tübke, Energy consumption of current and future production of lithium-ion and post lithium-ion battery cells, Nat. Energy 8 (2023) 1284–1295, https://doi.org/10.1038/s41560-023-01355-z.
[3] S. Kumar, P. Bora, P.C. Bhomick, D. Rangappa, D. Sinha, Graphene–MXene van der Waals heterostructures for high-performance supercapacitors, Nano Res. Energy 4 (2025) e9120148, https://doi.org/10.26599/NRE.2024.9120148.
[4] L. Yu, X. He, R. Liu, G. Wan, X. Ma, A. Pan, L. Shi, G. Zhang, Phosphorus incorporation-induced adsorption behavior modulation for carbon cathodes enables ultrastable and high-energy aqueous Zn-ion hybrid capacitors, Sci. China Chem. 68 (2025) 900–907, https://doi.org/10.1007/s11426-024-2293-9.
[5] J. Li, J. Zhang, L. Yu, J. Gao, X. He, H. Liu, Y. Guo, G. Zhang, Dual-doped carbon hollow nanospheres achieve boosted pseudocapacitive energy storage for aqueous zinc ion hybrid capacitors, Energy Storage Mater. 42 (2021) 705–714, https://doi.org/10.1016/j.ensm.2021.08.018.
[6] S. Yang, Y. Wang, H. Pan, P. He, H. Zhou, Lithium extraction from low-quality brines, Nature 636 (2024) 309–321, https://doi.org/10.1038/s41586-024-08117-1.
[7] A. Innocenti, S. Beringer, S. Passerini, Cost and performance analysis as a valuable tool for battery material research, Nat. Rev. Mater. 9 (2024) 347–357, https://doi.org/10.1038/s41578-024-00657-2.
[8] A. Yao, S.M. Benson, W.C. Chueh, Critically assessing sodium-ion technology roadmaps and scenarios for techno-economic competitiveness against lithium-ion batteries, Nat. Energy 10 (2025) 404–416, https://doi.org/10.1038/s41560-024-01701-9.
[9] X. Liang, J.Y. Hwang, Y.K. Sun, Practical cathodes for sodium-ion batteries: who will take the crown? Adv. Energy Mater. 13 (2023) 2301975 https://doi.org/10.1002/aenm.202301975.

[10] H. Ji, C. Xie, R. Zhang, H. Wu, J. Dai, S. Li, Q. Zhang, D. Sun, Y. Tang, P. Wang, T. Qiu, H. Wang, Sodiophilic interface and electrolyte regulation boost the lifespan of anode-free sodium battery, SusMat 5 (2025) e258, https://doi.org/10.1002/sus2.258.

[11] Y.J. Guo, R.X. Jin, M. Fan, W.P. Wang, S. Xin, L.J. Wan, Y.G. Guo, Sodium layered oxide cathodes: properties, practicality and prospects, Chem. Soc. Rev. 53 (2024) 7828–7874, https://doi.org/10.1039/d4cs00415a.

[12] J. Wang, Y.F. Zhu, Y. Su, J.X. Guo, S. Chen, H.K. Liu, S.X. Dou, S.L. Chou, Y. Xiao, Routes to high-performance layered oxide cathodes for sodium-ion batteries, Chem. Soc. Rev. 53 (2024) 4230–4301, https://doi.org/10.1039/d3cs00929g.

[13] W. Zuo, A. Innocenti, M. Zarrabeitia, D. Bresser, Y. Yang, S. Passerini, Layered oxide cathodes for sodium-ion batteries: storage mechanism, electrochemistry, and techno-economics, Acc. Chem. Res. 56 (2023) 284–296, https://doi.org/10.1021/acs.accounts.2c00690.

[14] B. Peng, Z. Zhou, J. Shi, X. Huang, Y. Li, L. Ma, Earth-abundant Fe-Mn-based compound cathodes for sodium-ion batteries: challenges and progress, Adv. Funct. Mater. 34 (2024) 2311816, https://doi.org/10.1002/adfm.202311816.

[15] J.Y. Hwang, J. Kim, T.Y. Yu, Y.K. Sun, A new P2-type layered oxide cathode with extremely high energy density for sodium-ion batteries, Adv. Energy Mater. 9 (2019) 1803346, https://doi.org/10.1002/aenm.201803346.

[16] J.U. Choi, J.H. Jo, Y.J. Park, K.S. Lee, S.T. Myung, Mn-rich P′2-$Na_{0.67}[Ni_{0.1}Fe_{0.1}Mn_{0.8}]O_2$ as high-energy-density and long-life cathode material for sodium-ion batteries, Adv. Energy Mater. 10 (2020) 2001346, https://doi.org/10.1002/aenm.202001346.

[17] H. He, D. Sun, Y. Tang, H. Wang, M. Shao, Understanding and improving the initial coulombic efficiency of high-capacity anode materials for practical sodium ion batteries, Energy Storage Mater. 23 (2019) 233–251, https://doi.org/10.1016/j.ensm.2019.05.008.

[18] A. Namazbay, M. Karlykan, L. Rakhymbay, Z. Bakenov, N. Voronina, S.-T. Myung, A. Konarov, Towards high-performance sodium-ion batteries: a comprehensive review on $Na_xNi_yFe_zMn_{1-(y+z)}O_2$ cathode materials, Energy Storage Mater. 77 (2025) 104212, https://doi.org/10.1016/j.ensm.2025.104212.

[19] G. Wang, J. Gao, W. Wang, Z. Tao, X. He, L. Shi, G. Zhang, Evoking surface-driven capacitive process through sulfur implantation into nitrogen-coordinated hard carbon hollow spheres achieves superior alkali metal ion storage beyond lithium, Battery Energy 2 (2023) 20230031, https://doi.org/10.1002/bte2.20230031.

[20] C. Ren, Y. Dong, Y. Lei, High-voltage cathode materials for sodium-ion batteries: advances and challenges, Small 22 (2026) 2501262, https://doi.org/10.1002/smll.202501262.

[21] X. Li, X. Sun, X. Hu, F. Fan, S. Cai, C. Zheng, G.D. Stucky, Review on comprehending and enhancing the initial coulombic efficiency of anode materials in lithium-ion/sodium-ion batteries, Nano Energy 77 (2020) 105143, https://doi.org/10.1016/j.nanoen.2020.105143.

[22] X. Yu, B. Liu, X. Yu, C. Wang, S. Zhang, L. Deng, Z. Wang, Towards high energy density transition metal oxide cathode for sodium – Ion batteries: a review on oxygen anionic redox strategy, Adv. Funct. Mater. 36 (2026) e16956, https://doi.org/10.1002/adfm.202516956.

[23] H. Ren, Y. Li, Q. Ni, Y. Bai, H. Zhao, C. Wu, Unraveling anionic redox for sodium layered oxide cathodes: breakthroughs and perspectives, Adv. Mater. 34 (2022) 2106171, https://doi.org/10.1002/adma.202106171.

[24] H. Xu, S. Guo, H. Zhou, Review on anionic redox in sodium-ion batteries, J. Mater. Chem. A 7 (2019) 23662–23678, https://doi.org/10.1039/c9ta06389g.

[25] B. Ku, H. Ahn, S. Lee, J. Ahn, M. Choi, J. Kang, H. Park, J. Kim, A.Y. Kim, H.-G. Jung, J.-K. Yoo, J. Kim, Stable high-voltage operation of oxygen redox in P2-type Na-layered oxide cathode at fast discharging via enhanced kinetics, Energy Storage Mater. 62 (2023) 102952, https://doi.org/10.1016/j.ensm.2023.102952.

[26] S.Y. Lee, H. Kweon, S. Lee, M.K. Cho, H. Ahn, J. Ahn, B. Ku, M. Choi, H.G. Jung, D. O. Shin, J. Kim, Enhanced fast-discharging performance and cyclability in oxygen-redox-based P3-type Na-layered cathode via vacancies in TM layers, Adv. Energy Mater. 14 (2024) 2402412, https://doi.org/10.1002/aenm.202402412.

[27] J. Ahn, J. Kang, M.K. Cho, H. Park, W. Ko, Y. Lee, H.S. Kim, Y.H. Jung, T.Y. Jeon, H. Kim, W.H. Ryu, J. Hong, J. Kim, Selective anionic redox and suppressed structural disordering enabling high-energy and long-life Li-rich layered-oxide cathode, Adv. Energy Mater. 11 (2021) 2102311, https://doi.org/10.1002/aenm.202102311.

[28] Y. Lee, H. Park, M.K. Cho, J. Ahn, W. Ko, J. Kang, Y.J. Choi, H. Kim, I. Park, W. H. Ryu, J. Hong, J. Kim, Li-rich Mn–Mg layered oxide as a novel Ni-/Co-free cathode, Adv. Funct. Mater. 32 (2022) 2204354, https://doi.org/10.1002/adfm.202204354.

[29] Y.J. Guo, P.F. Wang, Y.B. Niu, X.D. Zhang, Q. Li, X. Yu, M. Fan, W.P. Chen, Y. Yu, X. Liu, Q. Meng, S. Xin, Y.X. Yin, Y.G. Guo, Boron-doped sodium layered oxide for reversible oxygen redox reaction in Na-ion battery cathodes, Nat. Commun. 12 (2021) 5267, https://doi.org/10.1038/s41467-021-25610-7.

[30] X. Li, S. Yu, X. Zhao, J. Liu, Structural stability of layered oxides for sodium-ion batteries: insights and strategies, Energy Storage Mater. 79 (2025) 104303, https://doi.org/10.1016/j.ensm.2025.104303.

[31] X.-Y. Zhang, H.-Y. Hu, X.-Y. Liu, J. Wang, Y.-F. Liu, Y.-F. Zhu, L.-Y. Kong, Z.-C. Jian, S.-L. Chou, Y. Xiao, Expediting layered oxide cathodes based on electronic structure engineering for sodium-ion batteries: reversible phase transformation, abnormal structural regulation, and stable anionic redox, Nano Energy 128 (2024) 109905, https://doi.org/10.1016/j.nanoen.2024.109905.

[32] Y. Zou, X. Fu, Z. Zhao, B. Chen, Z. Zhu, W. Zuo, L. Zhang, W. Guo, Q. Xu, M. Ye, Unveiling Zn-induced reinforced transition metal-oxygen coupling in layered oxide cathodes for highly stable sodium-ion batteries, Nano Energy 142 (2025) 111179, https://doi.org/10.1016/j.nanoen.2025.111179.

[33] Y. Wang, X. Zhao, J. Jin, Q. Shen, Y. Hu, X. Song, H. Li, X. Qu, L. Jiao, Y. Liu, Boosting the reversibility and kinetics of anionic redox chemistry in sodium-ion oxide cathodes via reductive coupling mechanism, J. Am. Chem. Soc. 145 (2023) 22708–22719, https://doi.org/10.1021/jacs.3c08070.

[34] J.Y. Seol, O. Zhanadilov, M.-J. Cho, M.G. Kim, N. Voronina, S.-T. Myung, Coupled Fe^{3+}/Fe^{4+} and oxygen-redox chemistry in O3-type $Na[Li_{1/3}Fe_{1/3}Ru_{1/3}]O_2$ cathode for sodium-ion batteries, J. Power. Sources 676 (2026) 239837, https://doi.org/10.1016/j.jpowsour.2026.239837.

[35] X. Wang, L. Yin, A. Ronne, Y. Zhang, Z. Hu, S. Tan, Q. Wang, B. Song, M. Li, X. Rong, S. Lapidus, S. Yang, E. Hu, J. Liu, Stabilizing lattice oxygen redox in layered sodium transition metal oxide through spin singlet state, Nat. Commun. 14 (2023) 7665, https://doi.org/10.1038/s41467-023-43031-6.

[36] G. Kresse, J. Furthmüller, Efficiency of ab-initio total energy calculations for metals and semiconductors using a plane-wave basis set, Comput. Mater. Sci. 6 (1996) 15–50, https://doi.org/10.1016/0927-0256(96)00008-0.

[37] P.E. Blöchl, Projector augmented-wave method, Phys. Rev. B Condens. Matter. 50 (1994) 17953–17979, https://doi.org/10.1103/physrevb.50.17953.

[38] J. Perdew, K. Burke, M. Ernzerhof, Generalized gradient approximation made simple, Phys. Rev. Lett. 77 (1997) 3865–3868, https://doi.org/10.1103/PhysRevLett.77.3865.

[39] A. Jain, G. Hautier, S.P. Ong, C.J. Moore, C.C. Fischer, K.A. Persson, G. Ceder, Formation enthalpies by mixing GGA and GGA+U calculations, Phys. Rev. B 84 (2011) 045115, https://doi.org/10.1103/PhysRevB.84.045115.

[40] J. Heyd, G. Scuseria, M. Ernzerhof, Hybrid functionals based on a screened coulomb potential, J. Chem. Phys. 118 (2003) 8207–8215, https://doi.org/10.1063/1.1564060.

[41] A. Van der Ven, J.C. Thomas, Q. Xu, J. Bhattacharya, Linking the electronic structure of solids to their thermodynamic and kinetic properties, Math. Comput. Simulat. 80 (2010) 1393–1410, https://doi.org/10.1016/j.matcom.2009.08.008.

[42] S. Lee, W. Ko, H. Park, Y. Lee, J. Kang, J. Ahn, S. Lee, E. Sim, K. Ihm, K.-Y. Park, J. Kim, Gradational anionic redox enabling high-energy P2-type Na-layered oxide cathode, Chem. Eng. J. 451 (2023) 138883, https://doi.org/10.1016/j.cej.2022.138883.

[43] A. Urban, D.-H. Seo, G. Ceder, Computational understanding of Li-ion batteries, Npj Comput Mater 2 (2016), https://doi.org/10.1038/npjcompumats.2016.2.

[44] Q. Bai, L. Yang, H. Chen, Y. Mo, Computational studies of electrode materials in sodium-ion batteries, Adv. Energy Mater. 8 (2018) 1702998, https://doi.org/10.1002/aenm.201702998.

[45] B. Ku, J. Ahn, H. Lee, H. Ahn, J. Lee, H. Kweon, M. Choi, H.-G. Jung, K. Ihm, E. Sim, J.-K. Yoo, J. Kim, Enhancing structural flexibility in P2-type Ni-Mn-based Na-layered cathodes for high power-capability and fast charging/discharging performance, Energy Storage Mater. 74 (2025) 103930, https://doi.org/10.1016/j.ensm.2024.103930.

[46] J. Zhang, X. Li, Perspective on phase transition in layered oxide cathodes for sodium-ion batteries: mechanism, influenced factors, and inhibition strategies, Energy Fuels 38 (2024) 13906–13933, https://doi.org/10.1021/acs.energyfuels.4c02631.

[47] N. Yabuuchi, M. Kajiyama, J. Iwatate, H. Nishikawa, S. Hitomi, R. Okuyama, R. Usui, Y. Yamada, S. Komaba, P2-type $Na_x[Fe_{1/2}Mn_{1/2}]O_2$ made from earth-abundant elements for rechargeable Na batteries, Nat. Mater. 11 (2012) 512–517, https://doi.org/10.1038/nmat3309.

[48] C. Fu, J. Wang, Y. Li, G. Liu, T. Deng, Explore the effect of Co doping on P2-$Na_{0.67}MnO_2$ prepared by hydrothermal method as cathode materials for sodium ion batteries, J. Alloys. Compd. 918 (2022) 165569, https://doi.org/10.1016/j.jallcom.2022.165569.

[49] Y. Liu, S. Wang, W. Fu, S. Yao, Y. Ji, J. Li, L. Shi, X. Wang, F. Zhang, J. Yang, R. Liu, J. Xie, Z. Yang, Y.M. Yan, Oxygen edge-sharing strategy in P2-type $Na_{0.67}MnO_2$ cathodes: synergistic enhancement of intercalation kinetics and air stability, Adv. Funct. Mater. 35 (2025) 2420682, https://doi.org/10.1002/adfm.202420682.

[50] Q. Liu, W. Zuo, Z. Sun, G. Zeng, Y. Tang, K. Fang, D. Yu, K. Zhang, J. Li, Y. Hong, T. Qiu, N. Liu, C. Ouyang, X. Xiao, K. Amine, Z. Ning, Q. Zhang, G.-L. Xu, Y. Qiao, S.-G. Sun, Single-crystallization of O3-type layered oxide cathode for Na-ion battery, Chem. Mater. 37 (2025) 5874–5883, https://doi.org/10.1021/acs.chemmater.5c01106.

[51] D.D. Yuan, Y.X. Wang, Y.L. Cao, X.P. Ai, H.X. Yang, Improved electrochemical performance of Fe-substituted $NaNi_{0.5}Mn_{0.5}O_2$ cathode materials for sodium-ion batteries, ACS. Appl. Mater. Interfaces 7 (2015) 8585–8591, https://doi.org/10.1021/acsami.5b00594.

[52] Z. Lei, X. Luo, H. Liu, Y. Song, A. Shahid, R. Bao, X. Kong, Mg^{2+} dual-regulation strategy for O3-type sodium-ion battery cathodes: synergistic structural stabilization and dynamic charge compensation, Appl. Surf. Sci. 719 (2026) 165080, https://doi.org/10.1016/j.apsusc.2025.165080.

[53] H.J. Kim, A. Konarov, J.H. Jo, J.U. Choi, K. Ihm, H.K. Lee, J. Kim, S.T. Myung, Controlled oxygen redox for excellent power capability in layered sodium-based compounds, Adv. Energy Mater. 9 (2019) 1901181, https://doi.org/10.1002/aenm.201901181.

[54] Q.C. Wang, J.K. Meng, X.Y. Yue, Q.Q. Qiu, Y. Song, X.J. Wu, Z.W. Fu, Y.Y. Xia, Z. Shadike, J. Wu, X.Q. Yang, Y.N. Zhou, Tuning P2-structured cathode material by Na-site Mg substitution for Na-ion batteries, J. Am. Chem. Soc. 141 (2019) 840–848, https://doi.org/10.1021/jacs.8b08638.

[55] H. Wang, J. Qi, P. Jiao, Z. Wu, Z. Zhang, N. Jiang, D. Shi, G. Li, Z. Yan, K. Zhang, J. Chen, Core-shell structured P2-type layered cathode materials for long-life sodium-ion batteries, SmartMat 5 (2024) e1306, https://doi.org/10.1002/smm2.1306.

[56] Y. Shi, Z. Zhang, P. Jiang, A. Gao, K. Li, Q. Zhang, Y. Sun, X. Lu, D. Cao, X. Lu, Unlocking the potential of P3 structure for practical sodium-ion batteries by

fabricating zero strain framework for Na^+ intercalation, Energy Storage Mater. 37 (2021) 354–362, https://doi.org/10.1016/j.ensm.2021.02.020.
[57] B. Zhang, H. Ma, F. Tao, C. Lei, L. Zhang, C. He, M. Huang, Cation-anion co-redox induced high-capacity cathode for high energy density sodium-ion batteries, RSC Adv. 15 (2025) 12671–12676, https://doi.org/10.1039/d5ra01409c.
[58] Q. Zhou, Y. Li, S. Li, Z. Wang, Q. Li, X. Lu, Z. Qiu, C. Wu, Y. Bai, Ligand-field splitting parameter optimization achieves synergistic enhancement of transition metal redox activity and structural stability in high-voltage sodium layered oxide cathodes, Adv. Funct. Mater. 35 (2025) e09825, https://doi.org/10.1002/adfm.202509825.
[59] L.Y. Kong, J.Y. Li, H.X. Liu, Y.F. Zhu, J. Wang, Y. Liu, X.Y. Zhang, H.Y. Hu, H. Dong, Z.C. Jian, C. Cheng, S. Chen, L. Zhang, J.Z. Wang, S. Chou, Y. Xiao, A universal interfacial reconstruction strategy based on converting residual alkali for sodium layered oxide cathodes: marvelous air stability, reversible anion redox, and practical full cell, J. Am. Chem. Soc. 146 (2024) 32317–32332, https://doi.org/10.1021/jacs.4c04766.
[60] X. Lv, J. Liu, C. Li, F. Yu, D. Xiao, S. Zhao, Y. Wu, Y. Chen, Probing a solid electrolyte interphase layer with sub-nanometer pores using redox mediators, eScience 5 (2025) 100351, https://doi.org/10.1016/j.esci.2024.100351.
[61] Z. Wang, C. Tang, Z. Wang, Q. Zhang, P. Lv, K. Yu, J. Zheng, W. Wei, High-energy $Na_4MnCr(PO_4)_3$@C cathode for solid-State sodium metal batteries, Energy Mater. Adv. 4 (2023) 0036, https://doi.org/10.34133/energymatadv.0036.
[62] J. Zhang, Y. Wang, Y. Kang, H. Du, T. Jia, J. Xu, Y. Huang, Y. Zhao, F. Kang, B. Li, Cathode recycling of spent sodium ion batteries, Energy Mater. Adv. 5 (2024) 0128, https://doi.org/10.34133/energymatadv.0128.